CONVERGENCE AND SUBDUCTION AT THE NORTH EQUATORIAL FRONT

A THESIS SUBMITTED TO THE GRADUATE DIVISION OF THE UNIVERSITY OF HAWAII IN PARTIAL FULFILLMENT OF THE REQUIREMENTS FOR THE DEGREE OF

MASTER OF SCIENCE

IN

OCEANOGRAPHY

DECEMBER 1996

By

Michael Sawyer

Thesis Committee:

Pierre Flament, Chairperson
Doug Luther
Gary Barnes

We certify that we have read this thesis and that, in our opinion, it is satisfactory in scope and quality as a thesis for the degree of Master of Science in Oceanography.

THESIS COMMITTEE

Chairperson

Acknowledgments

The work described in this thesis was conducted in the framework of the Tropical Instability Wave Experiment. Funding was provided by the National Science Foundation (grants OCE-8818732, REU-8900858, OCE-8922207 and OCE-9117078) and the National Aeronautics and Space Administration (grant SIRC-093). This project provided a rich collection of data previously unavailable in any form, without which this work could never have been completed.

I wish to thank Pierre Flament, Gary Mitchum, Doug Luther, and Gary Barnes for serving on my Master's Committee and for their patient help in preparing this manuscript. In addition, Eric Firing, Roger Lukas, and Rudolf Kloosterziel provided valuable input on various aspects of this work.

The Physical Oceanography Graduate Student (POGS) group and Na'kama'kai, the graduate association in the Dept. of Oceanography provided invaluable support and input while preparing the oral defense and manuscript. In particular, Sean Kennan, Jim Potemra, Rick Lumpkin, Sophia Ashgar, Kathy Donahue, and Julia Hummon assisted in reviewing early drafts of this manuscript and listening to countless rehearsals of my oral defense.

It would be impossible to list everyone involved in the field research and initial data analysis of the Tropical Instability Wave Experiment, but their hard work was invaluable. Ken Shultis, Will Harvig, and Dave Gravatt of the University of Hawaii Shipboard Technical Operations Group and the crew of the *R/V Moana Wave* provided an excellent platform on which to collect these data. Acoustic Doppler Current Profiler data was collected with the support of Eric Firing's research group and analyzed by June

Firing. SeaSoar data was collected with the cooperation of the J. Luyten, W. Ostrum, and J. Thompson from the Woods Hole Oceanographic Institution and V. Lawford from Chelsea Instruments. The CTD system was maintained by Ken Constantine from the University of Hawaii. The Air-Sea Interactions package was designed by Pierre Flament, Uli Knirch, Ken Constantine, Bob Cunningham, Alton Goo, Hans Ramm, Mike Simpson, and Christian Trefois.

Finally, there are a number of people without which I would not even have become involved in oceanography to begin with. Charlie Johnson and Steven Reynolds at the North Carolina State University Dept. of Physics and John Morrison at the North Carolina State University Dept. of Marine and Atmospheric Sciences provided the early training and direction leading me to this work.

Presented in loving memory of Mack V. Sawyer II.

Abstract

Satellite thermal data from the equatorial Pacific show strong, seasonally dependent upwelling along the equator, characterized by a sharp front between the cold upwelling water and the warmer surrounding water to the north and south. Strong wave-like perturbations have been observed on this front, caused by meridional oscillations in response to the passage of Tropical Instability Waves, moving westward at 20 to 50 km/day with wavelength of 500 to 1000 km. This study, conducted in the framework of the Tropical Instability Wave Experiment, will focus on the small-scale dynamics of the front itself. Strong convergence is found in leading- and trailing-edge crossings of the front, resulting in subduction of the equatorial upwelling water below surrounding warmer waters, having potential significant impact on local biological processes. As the layer is subducted, a strong along-front jet is formed, moving to the east following the curvature of the front. Based on Temperature-Salinity properties of this jet, it serves to transport high-salinity water toward the north away from the equator, gradually mixing with surrounding water.

Table of Contents

List of Figures

List of Abbreviations

- ADCP Acoustic Doppler Current Profiler
- AVHRR Advanced Very High Resolution Radiometer
- CTD Conductivity, Temperature, and Depth profiler
- EqPac JGOFS Equatorial Pacific Leg
- EUC Equatorial Under-current
- GPS Global Positioning System
- ITCZ Inter-Tropical Convergence Zone
- JGOFS Joint Global Ocean Flux Study
- MCSST Multi-Channel Sea Surface Temperature
- MW9010 Moana Wave cruise 90-10
- MW9012 Moana Wave cruise 90-12
- NEC North Equatorial Current
- NECC North Equatorial Counter-current
- NOAA National Oceanic and Atmospheric Administration
- PMEL Pacific Marine Environmental Lab
- Ri Richardson Number

- SRL Shuttle Radar Laboratory
- SST Sea Surface Temperature
- TC9407 Townsend Cromwell cruise 94-07
- TIWE Tropical Instability Wave Experiment
- TS Temperature-Salinity
- SEC South Equatorial Current
- SRL Shuttle Radar Laboratory
- UTC Universal Time Code
- WOCE World Ocean Circulation Experiment

Chapter 1

Introduction

The objective of this thesis is to study the dynamics and thermohaline structure of the North Equatorial front, separating the Pacific equatorial upwelling water from the warmer tropical water to the north. High-speed sampling of temperature, salinity, velocity, and meteorological data was conducted in a number of frontal crossings, coupled with Lagrangian drifter studies, satellite thermography, and moorings in the vicinity of the front. Three specific regions will be discussed, as seen in Figure 1.1. The leading edge crossing refers to a crossing made on the western side of a perturbation in the North Equatorial Front, the trailing edge crossing was conducted on the eastern side of a perturbation, and the northern boxes were conducted at the northern extent of a perturbation.

1.1 Equatorial Current System Overview

Equatorial currents and water properties are strongly influenced by local atmospheric forcing. During the northern hemisphere winter, the Inter-Tropical Convergence Zone (ITCZ), located approximately between 5°N and 10°N is characterized by increased rainfall and reduced wind stress. The northeasterly trade winds lie to the north of the ITCZ and the southeasterly trades lie to the south.

The mean flow in this area consists of alternating regions of eastward and westward flowing currents, as seen in Figure 1.2 [Philander, 1990a]. The North Equatorial Current (NEC) and South Equatorial Current (SEC) are part of the anticyclonic current gyres of the north and south hemispheres, respectively. The NEC, located to the north of 10°N

has speeds generally less than 0.2 ms^{-1} westward. The SEC, located south of 3°N has a velocity reaching 1.0 ms^{-1} westward between the equator and 3°N, dropping to 0.1 ms^{-1} south of the equator. Between the NEC and SEC is the North Equatorial Counter-current (NECC), moving to the east with a velocity of around 0.5 ms^{-1}. The Equatorial Under-current (EUC) is a strong eastward-flowing jet with velocities reaching 1.50 ms^{-1} extending along the equator from around 50m depth to the permanent thermocline at around 150 dbar.

The Equatorial Pacific can be divided up into three distinct regions. From 90°W to 160°W is a region of strong upwelling driven by the divergence in the Ekman forcing as f changes sign along the equator. This upwelling region manifests itself as a tongue of cool water extending from the coast of South America toward the west, often reaching as far as the international date line [Cromwell, 1953; Cox, 1980]. Between 120°W and the date line, the upwelling becomes weaker, and the cold tongue becomes less prominent toward the west. West of the date line, the Western Pacific Warm Pool becomes the dominant feature of the region. This thesis will focus on the region between 90°W and 140°W.

Because equatorial surface currents are largely driven by wind stress curl from the trade-wind system, seasonal variation in the wind forcing will result in a similar variation in the strength of the equatorial currents. During periods of weakened southeast trades (Northern hemisphere spring), the equatorial surface currents are weakened. Reduced equatorial upwelling results from decreases in Ekman forcing. As the trade winds strengthen during Northern hemisphere fall, the surface currents increase and equatorial upwelling begins.

1.2 The North Equatorial Front

Sharp fronts are observed on the boundary between upwelling waters and warmer waters to the north and south. The North Equatorial Front is the boundary between the equatorial upwelling water and the warmer water to the north. Satellite Sea Surface Temperature (SST) images show temperature gradients of at least $1°\text{Ckm}^{-1}$, probably a low estimate limited by instrument resolution.

The amplitude of the front is largely a function of the magnitude of the upwelling. Figure 1.3 shows a series of satellite SST images collected May 7, May 26, and June 11, 1990. With the increase in northeast trades at the end of May, the upwelling is strengthened, increasing thermal gradients across the front. The strongest fronts are observed near the Peru coast, where the upwelling is greatest and the equatorial waters the coldest. Moving toward the west, upwelling is reduced, the cold tongue is weakened, and thermal gradients along the front are reduced. The dynamics west of the dateline are significantly different from those to the east, due to the influence of the warm pool on the surrounding waters.

1.3 Instabilities of the Equatorial Current System

Strong wave-like perturbations have been observed on the North Equatorial Front, caused by meridional oscillations in response to the passage of Tropical Instability Waves [Legeckis, 1977; Legeckis, 1986; Luther and Johnson, 1990; Johnson and Luther, 1994, and others]. These perturbations propagate westward at 20 to 50 km day^{-1} with meridional amplitudes reaching 500 km and zonal wavelengths of 500 to 1,000 km. Equatorial instabilities of this form were first observed in the Atlantic [Düing *et al.*, 1975], using

data from moored current meters. The first observation in the the Pacific was by Legeckis [1977] using satellite SST images. These perturbations contribute to the meridional eddy fluxes of momentum and heat playing a major role in the dynamical coupling of the currents in the equatorial current system.

Using a stability analysis of idealized equatorial currents, Philander [1978] suggests that the shear of the SEC or the shear between the SEC and NECC may be the primary source of instability. Hansen and Paul [1984] and Weisberger and Weingartner [1988] support this analysis using moored current meters and Lagrangian drifters. However, Cox [1980] and Hansen and Paul [1984] suggest that conversion of mean thermocline slope to eddy energy through baroclinic instability may play a role in generating tropical instability waves. Luther and Johnson [1990] find that barotropic instability between the SEC and EUC is most important during the boreal Summer, baroclinic conversions from 2-6°N during Winter, and baroclinic instabilities in the NECC thermocline most important during Spring.

1.4 Objectives of the Tropical Instability Wave Experiment

The Tropical Instability Wave Experiment (TIWE) was designed to test hypotheses of instability wave generation and interaction with zonal wave current systems in the Pacific and to understand the effects of the North Equatorial Front on the local oceanic and atmospheric environment. Previous field investigations have provided different views of the temporal and spatial structure of Instability waves; time series at a few fixed points, surface temperature, and synoptic velocity sections were often obtained as part of studies designed for different purposes. In contrast, TIWE was organized specifically to sample

the temporal and spatial progression of Equatorial Instability Waves over complete wave cycles.

Here we will focus on the structure of the equatorial front itself. Of special interest will be the northern crests of the perturbations, associated with poleward jets of cold haline water, which may play a significant role in meridional fluxes away from the equator. Mechanisms responsible for their growth and mixing properties will be discussed.

Convergence is required to maintain fronts in the ocean (or atmosphere). Thermohaline and velocity structures will be analyzed to quantify this convergence. Finally, connections to biological activity along the front will be explored.

The following points will be addressed:

- What is the thermohaline structure of the water column on either side of the front, and what dynamics are inferred from these thermohaline structures. In particular, can vorticity balances be applied.

- How strong is the surface convergence field along the front, and is it consistent in all regions.

- How is the biological activity in the region affected by these fronts? Do the fronts increase or decrease the productivity compared to that driven by the upwelling alone?

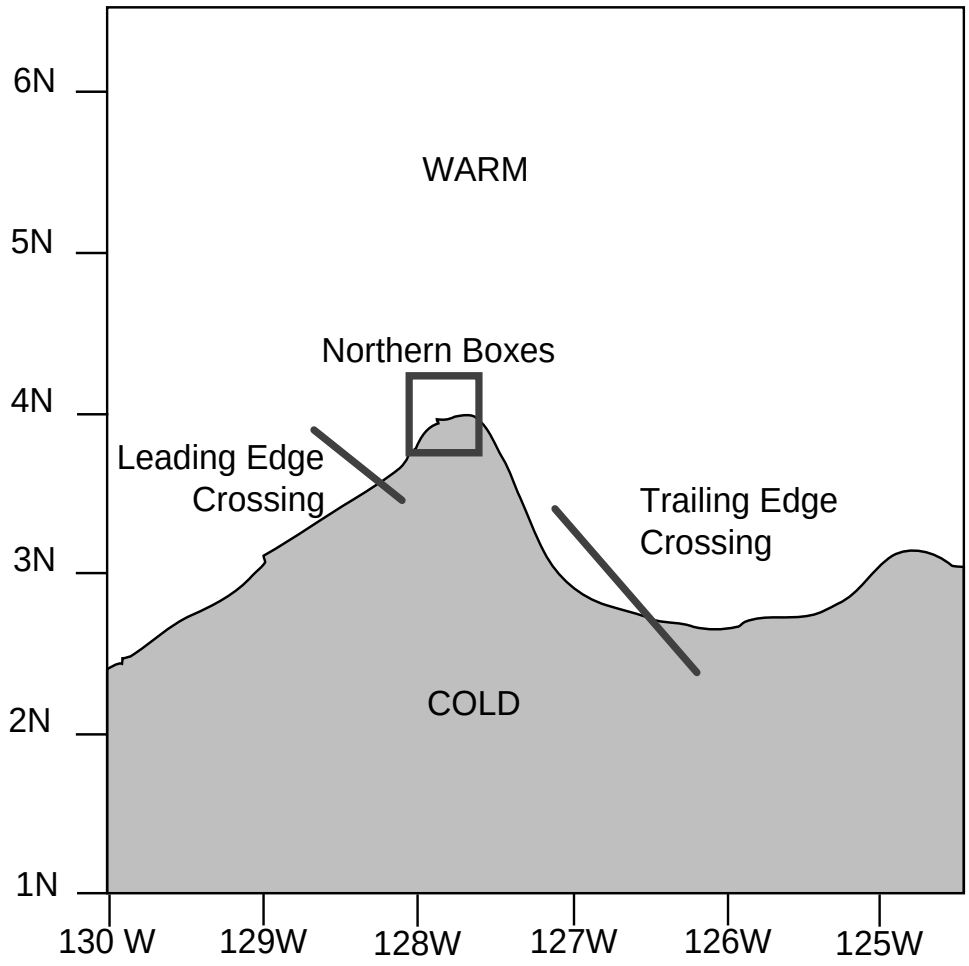

Figure 1.1: Schematic diagram of data used in this experiment. The gray area represents cold equatorial upwelling water and the white area represents warmer surrounding water. The location of the front is hand-traced from the satellite image on day 232, 01:59UTC, collected during the leading-edge crossing. The northern box and trailing-edge crossing have been translated at the phase speed of the perturbation. The leading-edge crossing was conducted in a line from the northwest to the southeast and the trailing-edge crossing was conducted from the southeast to the northwest. The northern boxes were conducted in alternating clockwise and counter-clockwise patterns.

Figure 1.2: A schematic diagram of the horizontal and vertical circulation in the tropical Pacific Ocean. *From Philander, et al. [1990b]*

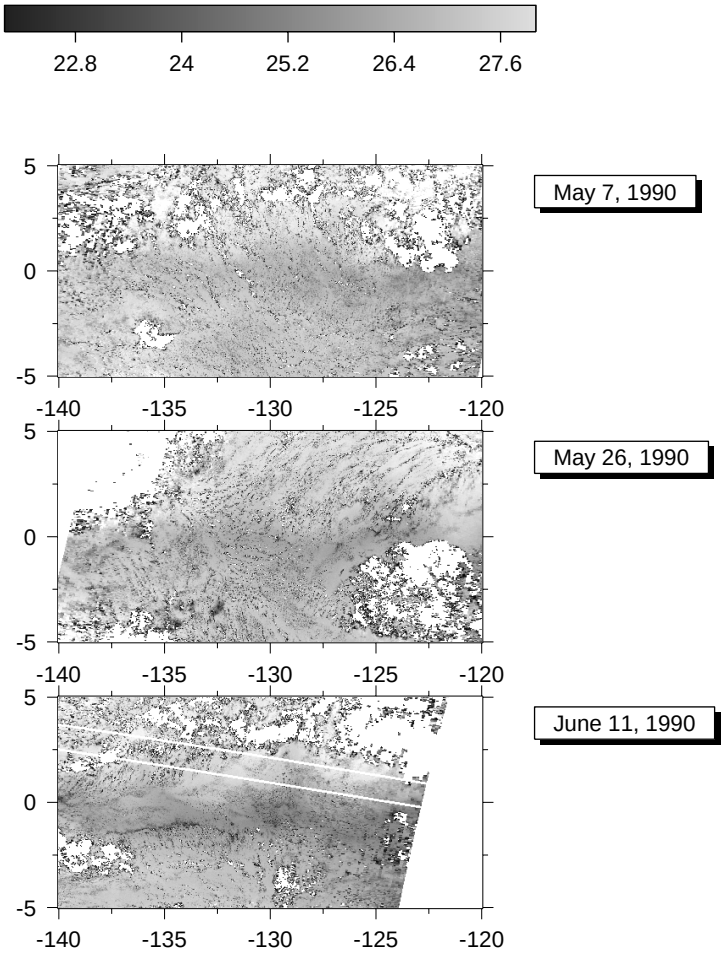

Figure 1.3: Series of satellite SST images of the Equatorial Pacific, showing increased upwelling strength during late Spring and early Summer, northern hemisphere. Dark shading represents cold water temperatures and light shading represents warmer temperatures. Upper frame was collected May 7, 1990, the middle frame was collected May 26, and the bottom June 11. The light band running horizontally across the figure is the equatorial upwelling region.

Chapter 2

Description of the Experiment

2.1 Field Programs

R/V Moana Wave cruise 90-10 (MW9010) in August, 1990, focused on the small-scale features of the North Equatorial Front itself. The sampling strategy during this cruise was driven by real-time analysis of satellite SST. Three closely spaced crossings were made on Aug 20 at 3.5°N by 129°W across a front in the western side of a perturbation (Figure 2.1). A 50 km counter-rotating box survey was conducted to coincide with a drifter launch at the northern tip of the perturbation at 4°N by 128°W. A single crossing of the front along the eastern side of the perturbation was conducted at 3°N by 127°W.

R/V Moana Wave cruise 90-12 (MW9012) in November, 1990, focused on the large scale dynamics of the equatorial instability. A 2° meridional by 3° zonal box survey (Figure 2.2) was conducted over the entire instability wave region, with a short excursion from the box pattern for a meridional sawtooth survey of the front in the region between two perturbations.

A series of cruises on the *R/V Thomas Thompson* were conducted in the TIWE region during the Joint Global Ocean Flux Study Equatorial Pacific (JGOFS EqPac) survey. This research was conducted to understand the biological implications of the North Equatorial Front [Yoder *et al.*, 1994]. Satellite data collected during this project will be discussed here, with a full treatment of the observations found in Johnson *et. al* [1996].

2.2 Instruments

During all field projects, Advanced Very High Resolution Radiometer (AVHRR) data from the NOAA polar orbiting satellites were collected from a shipboard receiving station. The Multi-Channel Sea Surface Temperature (MCSST) algorithm was used to produce maps of the SST over the TIWE study region; these data have a nominal resolution of 1.1 km, with highest resolution along the center of the satellite track, decreasing towards the edges. Gridded data were produced on a rectangular projection with a 1.25 km resolution. The North Equatorial Front was clearly seen in these data as a sharp boundary between the cold upwelling water and the surrounding water, nearly 2°C warmer.

During MW9010, Lagrangian drifters were deployed in the vicinity of the front in a spiral pattern to investigate the small-scale velocity field and to make estimates of frontal convergence rates. During MW9012, drifters were deployed at regular intervals throughout the cruise to investigate the large-scale velocity field.

World Ocean Circulation Experiment (WOCE) style "holey-sock" drifters were used in this project because of their tested ability to accurately follow the horizontal motions of water parcels [Niiler *et al.*, 1987; Niiler *et al.*, 1995]. Based on a mean wind velocity of 8 ms^{-1}, a velocity error of less than 0.01 ms^{-1} is expected using this drifter design. All drifters used were drogued at a mean depth of 15 m. Tracking during the cruise was provided directly by the on-board satellite receiver. A drifter mounted on the ship was used as a reference platform for these positions. Quality controlled data provided by Service ARGOS with a stated resolution of 300 m was used for post-processing and scientific analysis.

A 150 kHz shipboard-mounted Acoustic Doppler Current Profiler (ADCP) using a Global Positioning System (GPS) for navigation yielded velocity profiles to 300 m with an 8 m vertical resolution. Profiles were vector averaged in 5 minute ensembles, referenced against average ship velocity. A reference layer mean was removed from each profile before averaging and added back to the ensemble average. This prevented variations in ship's velocity from contaminating the estimated oceanic shear. Details on ADCP processing can be found in Firing *et al.* [1994].

A Conductivity, Temperature, and Depth (CTD) profiler was used during MW9010 and MW9012 to collect hydrographic data in the study area. Hydrographic casts were conducted to a depth of 300m, using dual temperature and conductivity sensors. Data were collected at 12 Hz during MW9010 and 24 Hz during MW9012, giving 12 and 24 samples per meter at the nominal lowering and raising rates of 1 ms^{-1}. Rates were reduced to 0.5 ms^{-1} in the vicinity of sharp gradients in any water property, such as the permanent 150 m thermocline. Niskin bottle samples were collected on alternate casts to ensure calibration accuracy. When bottle samples were collected one with the bottle as close to the surface as possible and one at 300 dbar pressure. Details on the CTD processing can be found in Trefois *et al.* [1993].

During MW9010, hydrographic stations were made along the frontal crossing on the eastern side of the perturbation, as well as on the return transect every $50 \sim 100$ km to 10°N. During MW9012, hydrographic stations were made at 25 km intervals along the ship track during the box survey.

In addition to conventional hydrography, a towed, undulating platform, the SeaSoar, was used to obtain continuous profiles of hydrographic data as the ship was underway. The SeaSoar was fitted with a conventional CTD profiler and yielded profiles from a

depth of 10 m to 300 m every 15 minutes at a ship velocity of 8 knots. Details on the SeaSoar deployment and processing are found in Appendix A.

During MW9010, the SeaSoar was deployed during the frontal crossing on the western side of the perturbation and during the box survey at the northern tip of the perturbation. During MW9012, the SeaSoar was used during some legs of the large box survey and during the sawtooth survey. Use of the SeaSoar was prevented by mechanical problems with the platform after day 330.

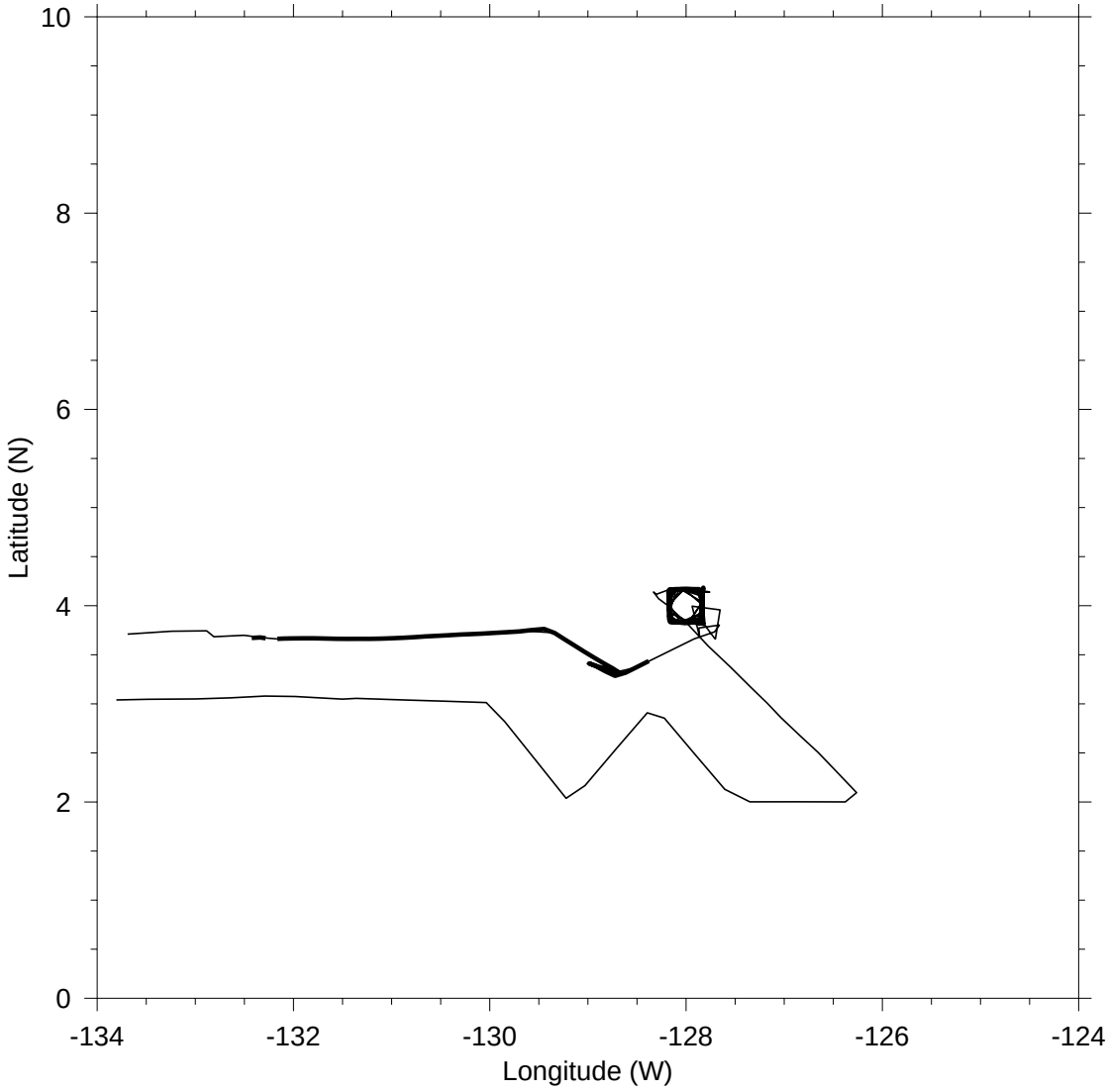

Figure 2.1: Ship track during MW9010.

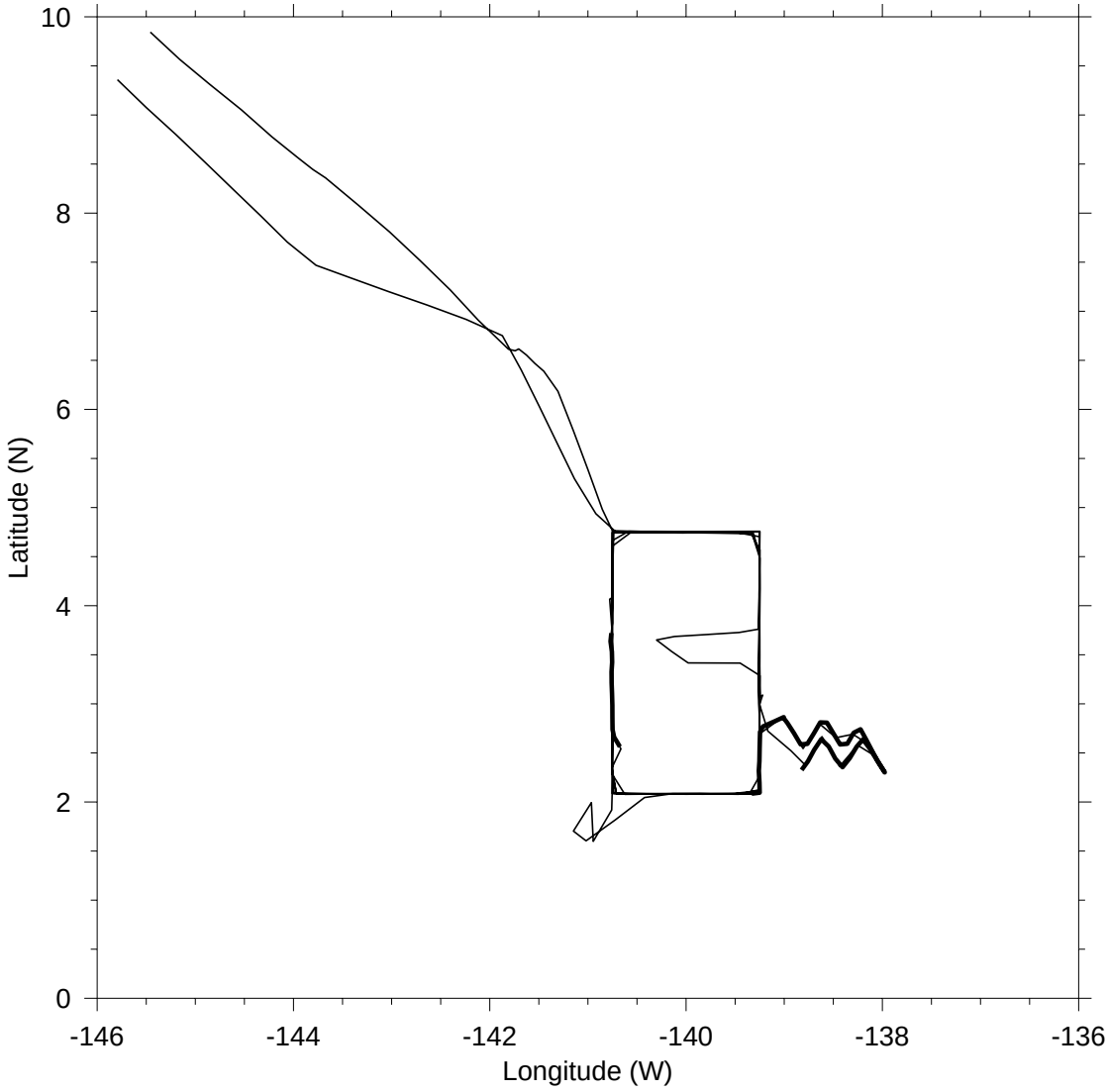

Figure 2.2: Ship track during MW9012.

Chapter 3

Large Scale Overview

A simplified view of a front between equatorial upwelling water and warmer water to the north or south is a line running zonally just off the equator. The actual front is subject to westward propagating perturbations, commonly referred to as "Tropical Instability Waves." To the first order, these perturbations can be viewed as a steady feature when observed in a frame of reference moving at their phase speed, suggesting that temporal variability of the front can be neglected. At higher orders, however, the leading edge of the front gradually tilts with time because of the meridional variation in phase speed. The sharpness of the front is not affected by these variations; thermal gradients on the order of 1°C km^{-1} are found in nearly all observations of the front during the study period.

3.1 Sea Surface Temperature Fields

The most obvious signature of the perturbations in the North Equatorial Front are seen in the SST field inferred from satellite data, collected during MW9010, MW9012 and JGOFS.

3.1.1 MW9010

Figure 3.1a shows a series of successive satellite images collected during MW9010 between August 20, 1990 and August 23, 1990. Figure 3.1a is typical of the North Equatorial Front during the instability wave season. A strong front is seen oriented southwest to northeast starting at 2°10′N 130°W. Water to the southeast side of the front was

nearly 2°C colder than to the northwest. At 3°5′N 128°W, the front turns sharply to the east, continuing directly zonal until 127°30′W, where it angles toward the south, weakening slightly. By 126°20′W, it has gradually returned to a zonal orientation, at around 3°5′N. The leading edge of the front between 2°N and 4°N forms a nearly straight line with an orientation of 40°. Throughout this time period, the leading edge of the front manifested itself as a nearly straight line over at least 200 km, with thermal gradients larger than $1°\text{Ckm}^{-1}$.

Figure 3.2 shows the position of the leading edge front, hand-extracted from the images. Figure 3.3 shows the location of the front at 2, 2.5, and 3°N as a function of time. From these data, a phase speed of 0.51 ± 0.11 ms^{-1} is found at 2°N. This is a function of longitude; at 2.5°N, the phase speed is 0.55 ± 0.10 ms^{-1} and at 2°N it is 0.58 ± 0.26 ms^{-1}. This suggests a meridional variation in propagation speed of the perturbation, probably in response to the mean current shear between the NECC and NEC. Therefore, the orientation of both leading and trailing fronts changes with time. As the leading edge becomes more zonally oriented, the trailing edge becomes more meridionally oriented, until the perturbation becomes unstable, and appears to collapse under the shear between the NECC and NEC.

3.1.2 JGOFS

Figure 3.4 shows a series of SST images collected during JGOFS. The equatorial upwelling is clearly visible along the equator as a band of cold water stretching from around 3°S to 3°N, with a sharp perturbation visible at 133°W. As in MW9010, the leading edge front is at least $1°\text{Ckm}^{-1}$. To the west of the peak in the first image (collected on day 224), the leading edge front is oriented nearly zonal before bending to a

more meridional orientation. The trailing front is oriented nearly meridional, with the southern extent further to the west than the northern tip.

By day 224 (Figure 3.4a), the tip was beginning to shear to the east, with the southern extent of the trailing front well to the west of the northern tip. A band of clouds was seen just to the west of the leading edge front and to the east of the trailing edge, suggesting interactions between local atmospheric dynamics and the oceanic front.

By day 230 (Figure 3.4b), the northern tip of the perturbation is no longer clearly visible. The southern extent was more zonally oriented as leading edge front had moved northward. Again, there was a sense of preferential cloud development on the north side of the front.

By day 234 (Figure 3.4c), the tip of the perturbation has been completely removed, and the perturbation has resumed the shape similar to that seen during MW9010. To the north of the "main" perturbation and front was a secondary front with smaller scale perturbations, at around 5°N. This front likely existed throughout all images, but was not visible because of cloud cover in previous images.

3.2 Three-Dimensional Views of the fronts

Since the propagation of the perturbations can be successfully tracked, it is possible to construct a three-dimensional view of the perturbation, moving all data collected into a common space-time frame. [Flament *et al.*, 1996]

3.2.1 JGOFS front

Figure 3.5 shows a perspective view of the three-dimensional equatorial temperature field in August 1992, looking towards the north west. The surface temperature is derived

from a satellite infrared image acquired by the shipboard receiving station. The vertical face is from a series of CTD stations. The south and east faces are painted with temperature data from the PMEL/TAO and USC moorings. Clouds in the ITCZ are painted in perspective, using satellite-derived cloud top temperature as a proxy for height. All data (satellite, ship, moorings) have been translated to the common time of 28 August 1992, using a uniform westward phase speed of 71 cms^{-1} for the front, inferred from the sequence of images in Figure 3.4.

The view reveals the upwelling tongue along the equator, distorted by the passage of a large amplitude Tropical Instability Wave. The leading edge of the wave was crossed by the ship at about 3°30′N; the corresponding temperature front was confined to the mixed layer, with no signature below the thermocline. The crest of the wave, extended northward to about 5°30′N as a narrow filament of cold water.

3.2.2 MW9012 front

Figure 3.6 shows a perspective view of the three-dimensional temperature and surface velocity field during MW9012. All available data from shipboard observations, drifting buoys, and moorings were used to produce this figure, translated into a moving frame of reference moving with the perturbation westward at 0.3 ms^{-1}. [Flament *et al.*, 1996]

The horizontal velocity field reveals an anticyclonic eddy of 250 km radius stationary in the moving frame of reference. The eddy was trapped between the NECC at around 6°30′N and the SEC at around 2°30′N. Cold equatorial water was advected toward the north along the western side of the eddy and warm water to the south along the eastern edge. The center of the eddy corresponded to the boundary between the cold water to the west and the warm water to the east. The eddy was confined to the upper water

column; below the equatorial thermocline at around 150 dbar, velocities associated with the eddy were less that 0.1 ms^{-1}, compared with with velocities around 0.5 ms^{-1} above the thermocline. The northward flow of cold water was generally shallow, confined to the upper 75 dbar, with a maximum flow of 0.6 ms^{-1} while the southward return flow was generally deeper, centered around 75 dbar. The thermocline deepened significantly near the center of the eddy (central cut of Figure 3.6), suggesting that the eddy was consistent with a geostrophic balance.

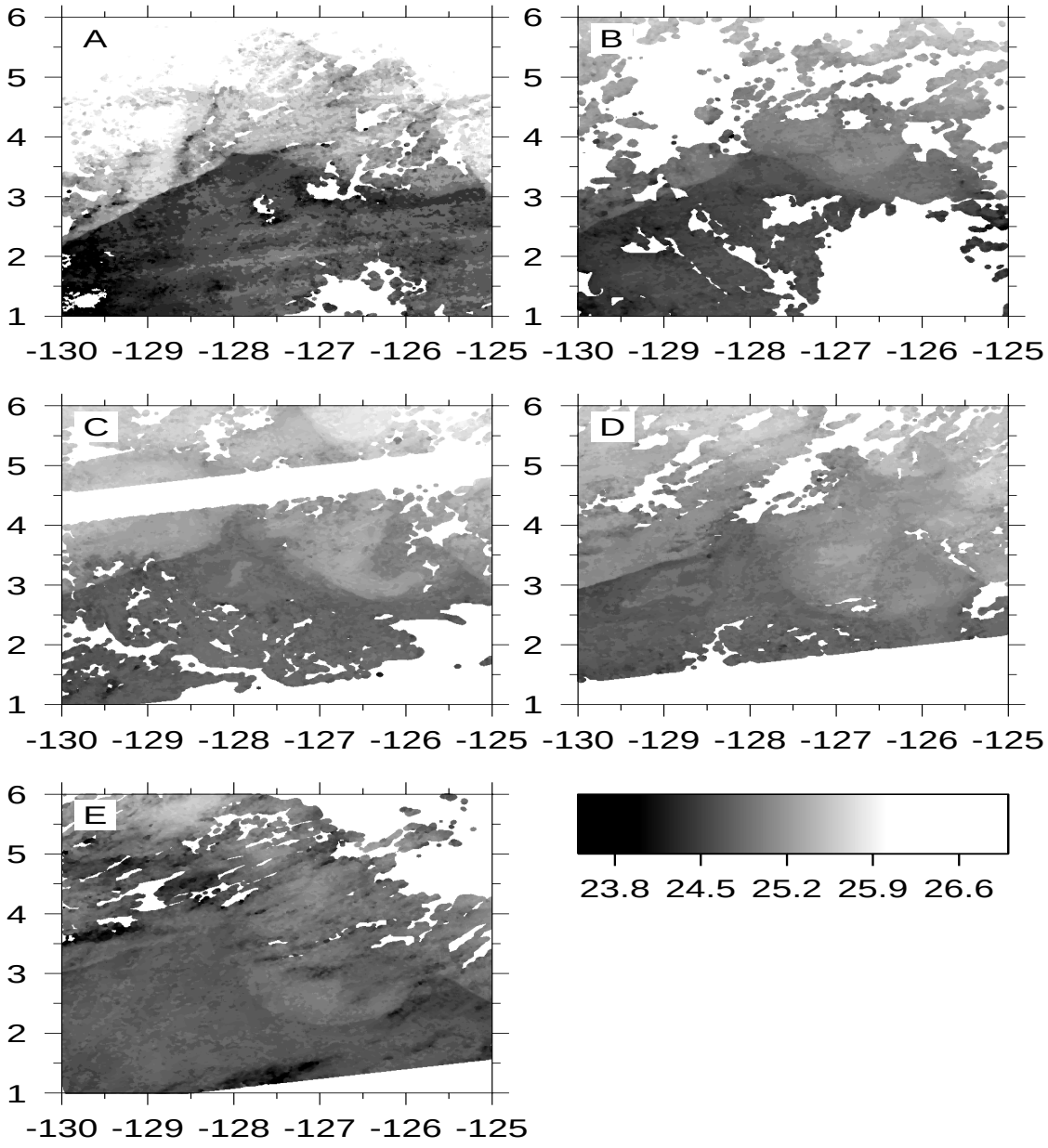

Figure 3.1: Series of satellite SST images collected during MW9010. Images were collected on (a) Aug 20, 1990, 01:59 UTC, (b) Aug 21, 01:41, (c) Aug 21, 22:30, (d) Aug 22, 22:19, and (e) Aug 23, 22:08. Note the gradual change in angles of the leading and trailing edge fronts.

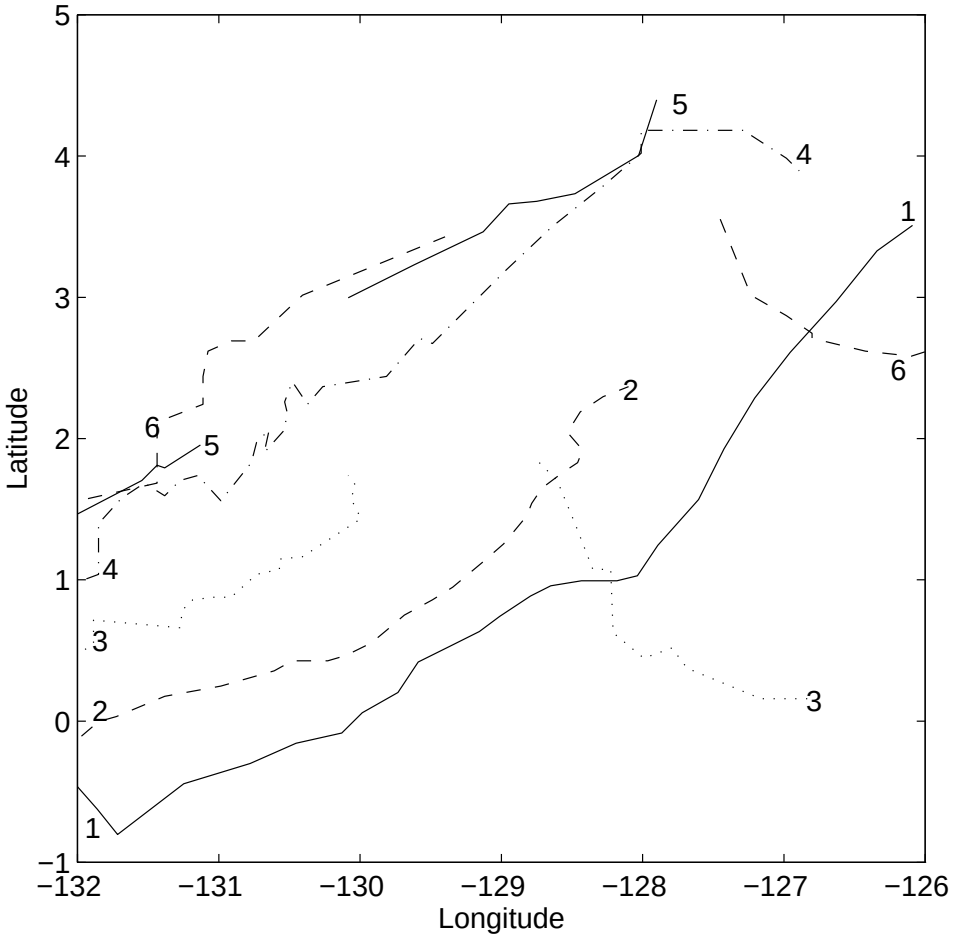

Figure 3.2: Frontal locations during MW9010, based on hand-location from satellite SST images. The earliest data is to the east in the image, and the front propagates toward the west. Line 1 (solid) was collected Aug 13, 10:10 UTC, line 2 (dashed) Aug 15, 10:54, line 3 (dotted) Aug 17, 10:28, line 4 (dash-dot) Aug 19, 10:06, line 5 (solid) Aug 21, 22:30, line 6 (dashed) Aug 22, 22:19.

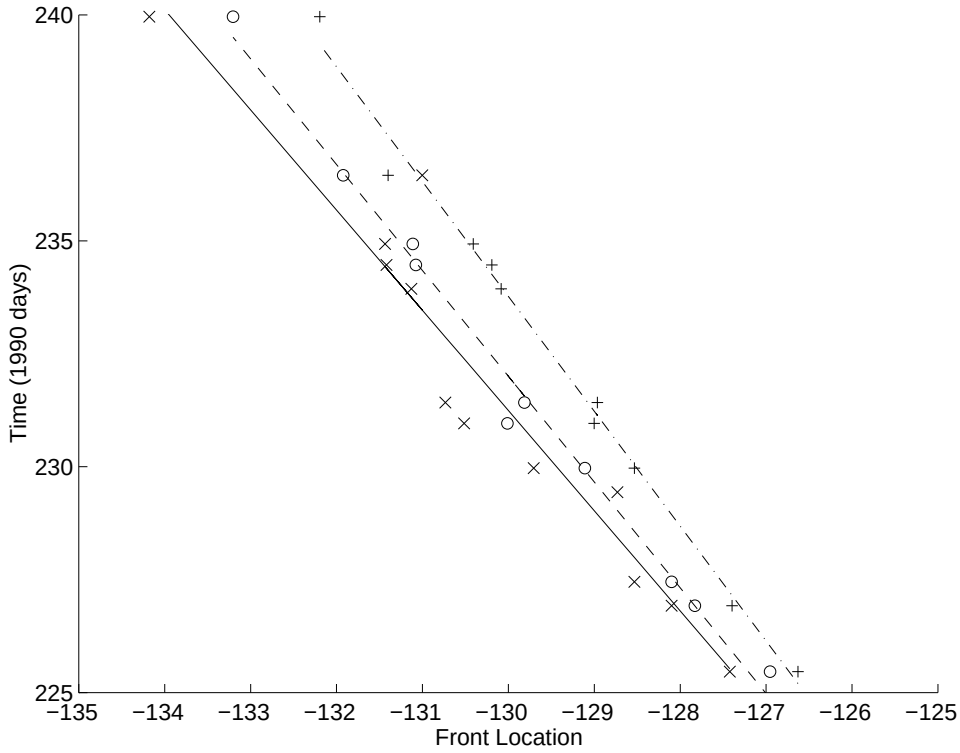

Figure 3.3: Phase speed of front motion at three locations during MW9010, based on frontal locations from Figure 3.2. A phase speed of 0.58 ms^{-1} was found at 2°N, indicated by the solid line with individual points indicated by '×' symbols. A phase speed of 0.55 ms^{-1} was found at 2.5°N, indicated by a dashed line and the '○' symbol, and a speed of 0.58ms^{-1} was found at 3°N indicated by dash-dotted line and the '+' symbol.

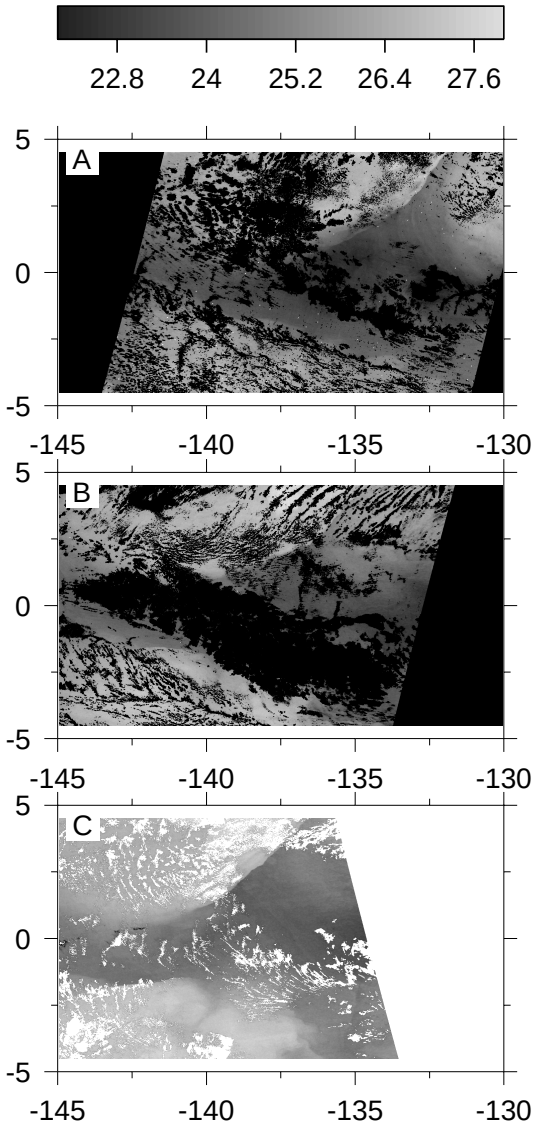

Figure 3.4: Series of satellite SST images collected during JGOFS. Images were collected (a) Aug 11, 1992, 12:08 UTC, (b) Aug 17, 12:36 UTC, and (c) Aug 21, 00:44 UTC. Note the gradual change of the jet-like feature at the northern tip of the perturbation.

Figure 3.5: Perspective view of the three-dimensional temperature field from data collected during JGOFS. The top face is derived from satellite SST measurements, the south and east faces are taken from data collected by PMEL/TAO and USC moorings, and the slice along the center is from shipboard hydrography. Clouds are painted above the satellite image using cloud-top temperature as a proxy for cloud height. The equator is indicated with a dashed line.

Figure 3.6: Perspective view of the three-dimensional temperature field from MW9012.

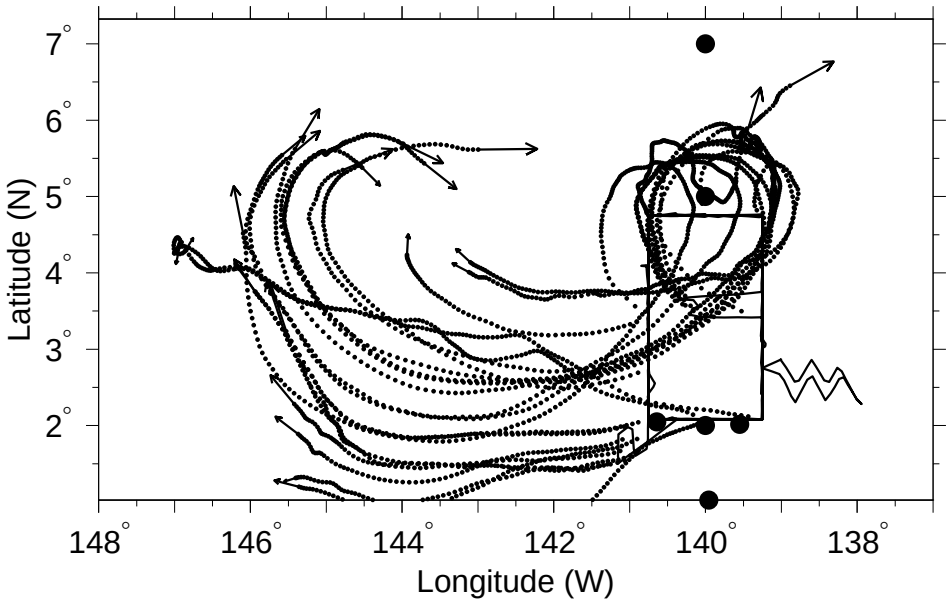

Figure 3.7: Trajectories of drifting buoys between Nov. 17 and Dec. 5, 1990, shown every 6 hours. The end of each trajectory is marked by an arrow. The ship track during MW9012 is overlayed in a solid line, with the moorings marked with solid circles. *From Flament,* et al. *[1996]*

Chapter 4

The Leading Edge of the Wave

During MW9010, a series of three closely-spaced transects were completed across the leading edge of a perturbation in the North Equatorial Front. The location of these transects is shown in Figure 1.1. Based on satellite SST data, the front was determined to be oriented at 40°. The section was conducted at nearly a right angle to the front, and all data have been rotated into an along-front and across-front coordinate system. Data from this section will be used to estimate rates of convergence and subduction along the North Equatorial Front, and used to identify a high-salinity along-front jet.

4.1 Convergence and Subduction

Figure 4.1 shows the average across-front velocity and temperature fields from these sections. These data are given in terms of the along-track distance from the front, negative values indicating data to the southeast of the front, positive values to the northwest. To the southeast of the front, temperature was nearly constant from the surface to the permanent 150 dbar thermocline, with a temperature of around 24.8°C. In the upper 75 dbar, the water was moving toward the front to the northwest with a velocity of around 0.4 ms^{-1}. Between 75 dbar and the 150 dbar thermocline, the water was nearly stationary. On the northwest side of the front, an intermediate "subduction" thermocline was seen at a depth of around 75 dbar. Above this subduction thermocline water was considerably warmer than the water to the south, with temperatures in excess of 26°C. Across-front velocity in the upper layer was nearly zero, with the lower layer moving toward the northwest, away from the front, at a velocity of around 0.3 ms^{-1}.

The surface flow on the southeast side of the front was subducted below the stationary layer to the northwest. The thickness of the moving layer does not change significantly from 75 m.

The change in surface velocity at the location of the surface front was significant: 0.5 ms^{-1} over a distance of 10 km, suggesting a surface convergence rate of $5 \times 10^{-5} s^{-1}$. Similarly, there was a change in across-velocity just above the 150 dbar thermocline of 0.4 ms^{-1} over a distance of around 40 km, suggesting a divergence rate of around $1 \times 10^{-5} s^{-1}$.

The front was straight over a distance of nearly 300 km, with consistent along-front SST gradients over this distance, suggesting that the front is spatially invariant along its length. Significant along-front variations would likely result in a gradual change in curvature of the front or along-front changes in the SST gradient, which are not observed.

Assuming along-front invariance, the horizontal divergence field can be produced (Figure 4.2a). This field shows convergence along the subduction, extending 30 km to the northwest. Figure 4.2b shows vertical velocity calculated from this divergence field, obtained by integrating divergence downward from the surface. Downwelling as high as 10^{-3} ms^{-1} is observed along the region of subduction.

4.2 Along-Front Jet

Figure 4.3a shows the along-front velocity measured during the leading-edge transect with the temperature field overlayed. A jet was observed between the subduction thermocline and the 150m thermocline, flowing toward the northeast at a velocity reaching 0.8 ms^{-1}. Figure 4.3b shows the salinity field from this section. The along-front jet

observed was at the same temperature as the subducted water, but had salinities in excess of 35.1 at the core. A slight deepening of the 150 dbar thermocline in the area of this jet was seen, with no significant signal observed below the thermocline.

4.3 Biological Properties

Recent studies [Flagg and Smith, 1989] have linked such an increase in backscatter amplitude with increases in biomass in the water column. It is also clear that the increase in scattering extends below the thermocline (about 150 dbar). Two possible explanations for this both result from the falling of dead organic material through the thermocline. This organic material itself can serve as additional scattering sources while falling, or there can be increased microorganisms in this region using the falling organic material as a food source.

Yoder *et. al.* [1994] describe a mechanism for concentrating *Rhizosolenia* near the frontal convergence. Visual observations during all field projects support this hypothesis; both biological and man-made material are observed to accumulate along the front.

Due to migration of plankton, changes in the scattering properties can be attributed to this diurnal cycle as well as spatial variations in productivity. Data for the leading edge crossing were collected between 06:00 UTC and 14:00 UTC, corresponding to between 20:00 and 4:00 local time, with the frontal crossing itself at around 2:00 local time. Because the migrations of phytoplankton are primarily associated with changes in incident light, it is not expected that diurnal variations are playing a significant role in the observed scattering pattern.

Normalized ADCP scattering data can be used to measure this backscatter. These data (Figure 4.4) suggested concentration of biological activity on the southern side

of the front in the upwelling region. Although no direct biological data was collected, this is consistent with the assumption that the upwelling region is an area of increased productivity.

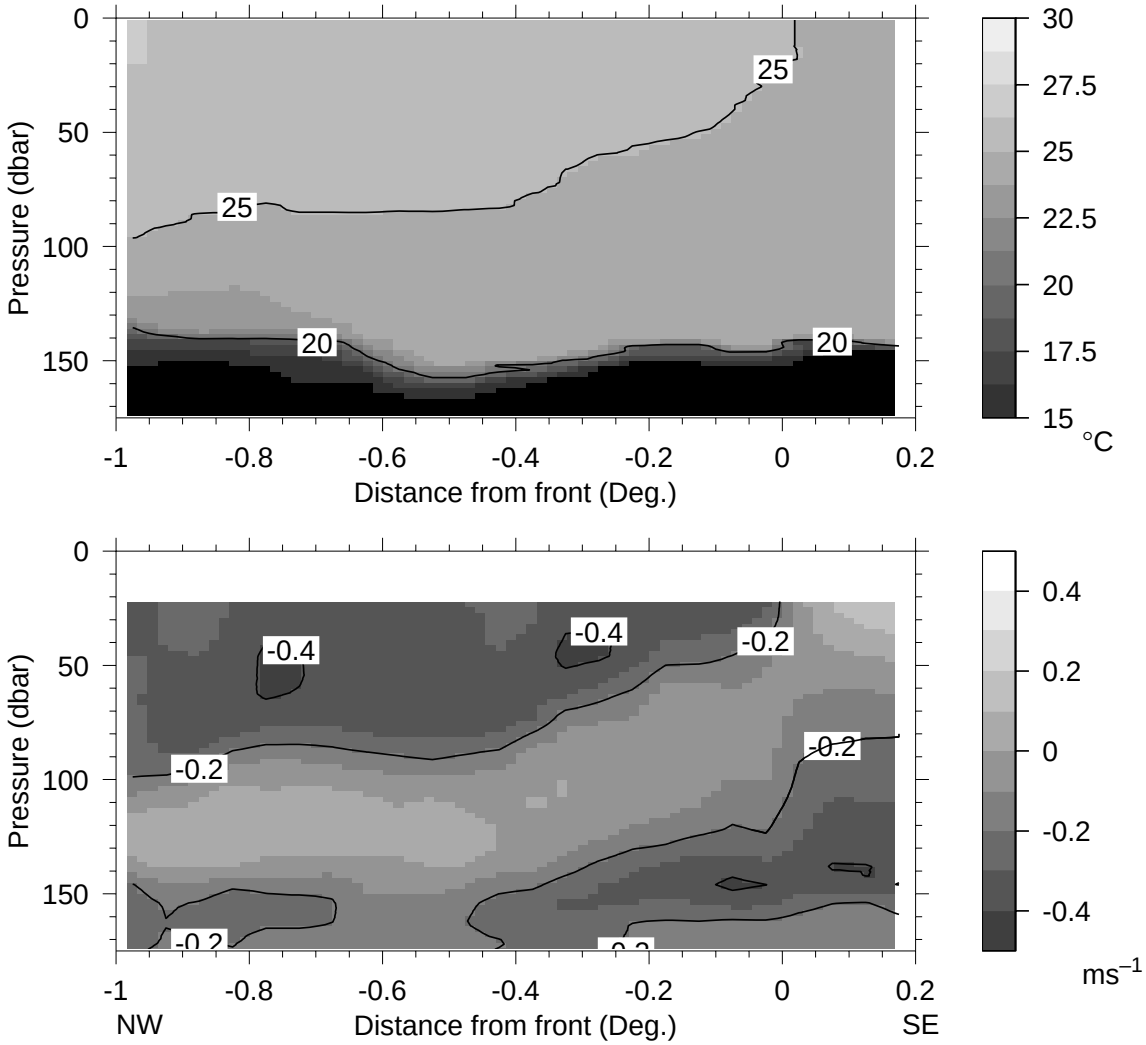

Figure 4.1: Temperature (upper panel) and across-front velocity (lower panel) of leading edge front crossing. Temperature contours are shown every 5°C with grayscale changes every 1.25°C. Velocity contours are shown every 0.2ms^{-1} except at $0\ \text{ms}^{-1}$ with grayscale changes every 0.1ms^{-1}.

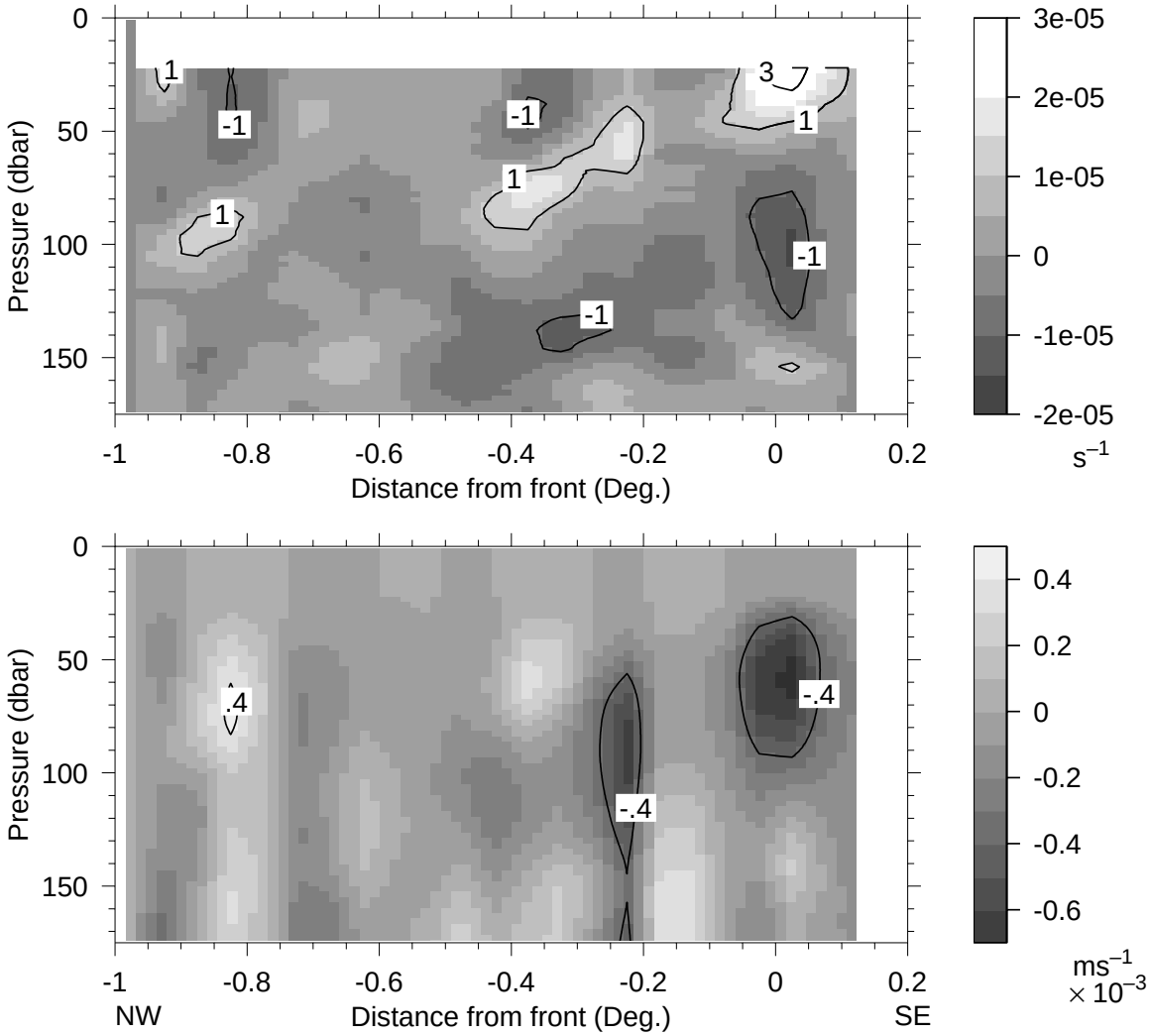

Figure 4.2: Divergence (upper panel) and vertical velocity (lower panel) of leading edge front crossing. Divergence contours are shown every 2×10^{-5} sec^{-1} with grayscale changes every 0.5×10^{-5} sec^{-1}. Velocity contours are shown at $\pm 0.4 \times 10^{-3}$ ms^{-1} with grayscale changes every 0.1×10^{-3} ms^{-1}.

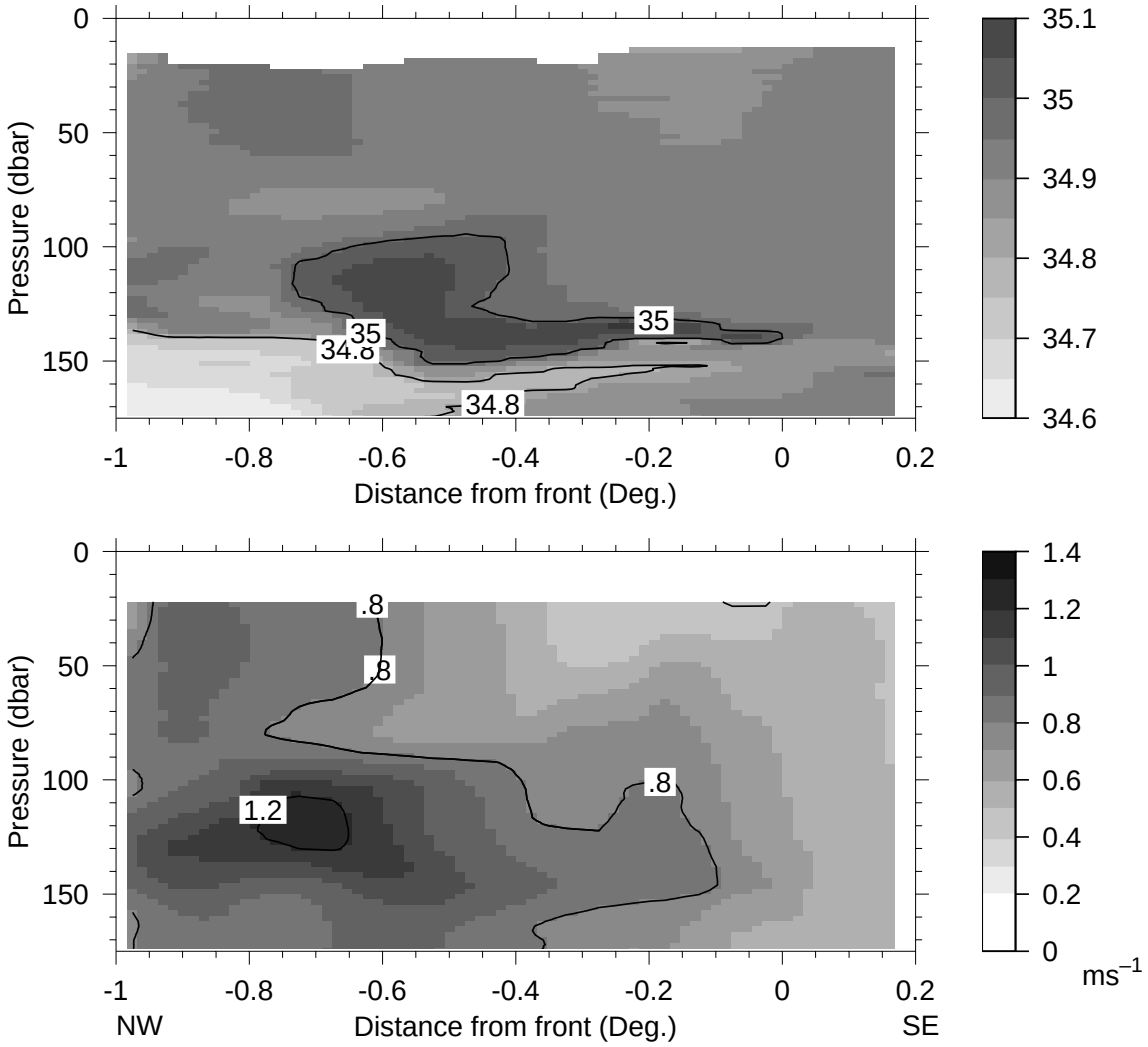

Figure 4.3: Salinity (upper panel) and along-front velocity (lower panel) of leading edge front crossing. Salinity contours are shown every 0.2 with grayscale changes every 0.1. Velocity contours are shown at 0.4 ms^{-1} with grayscale changes every 0.1 ms^{-1}.

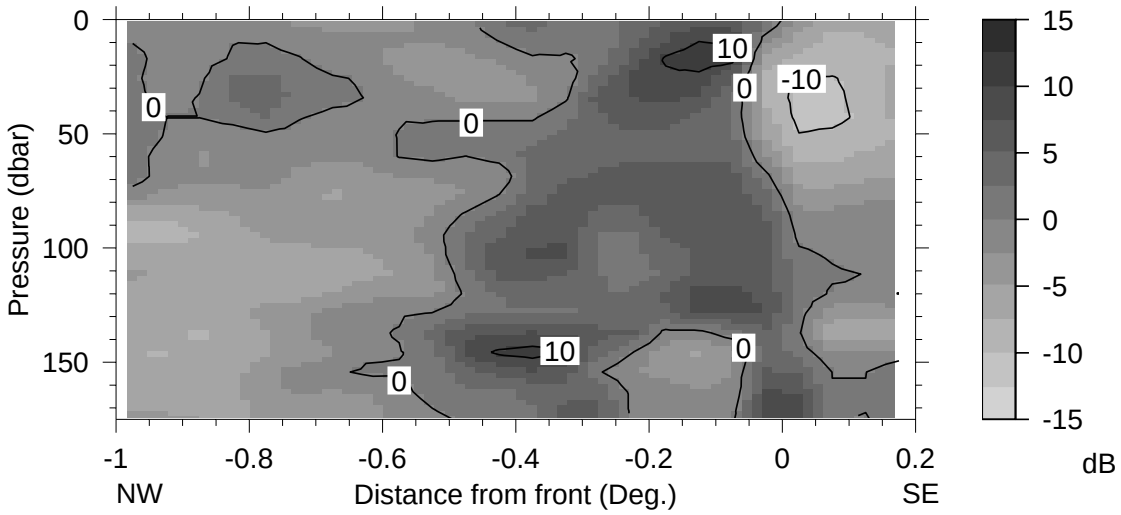

Figure 4.4: ADCP Backscatter amplitude from leading-edge crossing in dB. Dark shades indicate increased backscatter with contour intervals every 10 dB and grayscale increments every 2.5 dB. The mean depth profile has been removed from these data.

Chapter 5

Northern Tip of Wave

During MW9010, an array of drifters was deployed in the vicinity of the northern tip of the perturbation. In addition, a counter-rotating box survey was conducted using SeaSoar and ADCP. These data were used to understand the velocity structure and water types at the northernmost extent of the perturbation.

5.1 Drifter Convergence

The drifters released during MW9010 were initially deployed in a spiral pattern; figure 5.1 shows a time-series of the drifter positions interpolated between fixes to a regular time interval. The zero lines on each frame correspond to the mean location of the entire drifter field. The convergence at the front is clear; by day 237.5, the drifter field had collapsed into a line oriented along an observed SST front, with the exception of a single drifter which moved rapidly to the northwest.

Focusing on the inner group of the spiral, principle component analysis on the displacement of individual drifters from a mean position was conducted. Representing the component axes using an ellipse, this method can be used to approximate the change in area of the drifter array. The outlying drifter is not included in the ellipse calculation, and indicated by an "$\circ$" in the figure. Figure 5.2 shows a time-series of the area of the ellipse. The rate of convergence from this change of area, given by $\frac{1}{\mathbf{A}}\frac{\Delta \mathbf{A}}{\Delta t}$, was found to be $7 \pm 1.4 \times 10^{-5}\mathrm{s}^{-1}$. Error is given as one standard deviation found using a 100,000-run bootstrap technique, repeating the principle component analysis over a randomly selected sample of available drifters.

5.2 Box Survey

After the drifters were deployed, a series of transects were conducted in a 50 km square box pattern. The direction of rotation in the box pattern was periodically reversed, to prevent aliasing of tides. Figure 5.3 shows successive maps of currents at 25 dbar depth, determined from drifters and the ADCP. As in the drifter plots, time samples at each grid location were linearly interpolated between successive passages at that location with the ship.

Figure 5.4 shows the time-series of divergence calculated from these data by integrating over the flow across the boundary of the box. As the perturbation passes into the box, the convergence rate increases to around $-8 \times 10^{-6}\mathrm{s}^{-1}$, comparable to the rate of divergence found from the collapse of the drifter field. The vorticity found by integrating circulation around the box is shown in Figure 5.5, suggesting strong negative vorticity (-6×10^{-6}) leading the tip of the perturbation, decreasing to nearly zero as the perturbation passed. The divergence and vorticity fields from the box survey changed sign at the same time at around yearday 236.5, suggesting that the vorticity field was connected to the divergence, thus the vertical velocity field. In the vicinity of the front, a positive vorticity was observed, but away from the front, as the field became divergent, the circulation was reversed.

5.3 Velocity Field

Figure 5.3 shows velocity inferred from the drifters and box surveys combined together. The initial drifter deployment (day 234) suggested strong anti-cyclonic motion of the drifters, particularly in the northern segments, as expected from the vorticity calcula-

tions from the box survey. By day 235, the front was clearly visible along the southern face of the box as a sharp change in velocity at 128°W, and along the eastern face as a change at 4°N. By this time, the drifters had accumulated in a line joining the two frontal crossings observed in the box survey.

By day 236, the leading edge of the perturbation had nearly left the box and the trailing edge was clearly visible in the southern edge of the box as sharp change in velocity along the south side of the box. The drifters had separated into two groups; most falling along the trailing edge of the front with a few along the leading edge. Both the velocity field along the southern face of the box and the convergence of drifters suggested that both the leading and trailing edge of the perturbation were convergent. The two convergent zones meet at around 4°N by 127°55′W, continuing northward as a jet clearly seen in the northern face of the box at 128°55′W. By day 236.50, a single drifter was seen trapped in this jet, moving to the north.

For the remainder of the time-series, the perturbation continued to steadily propagate to the west, occasionally loosing drifters out the northward-flowing jet. Behind the perturbation, the velocity was strongly westward, compared to a southward velocity in the leading edge (best seen on day 237.5). Thus, the northward jet served as a front between strong southward velocity to the west and westward velocity to the east.

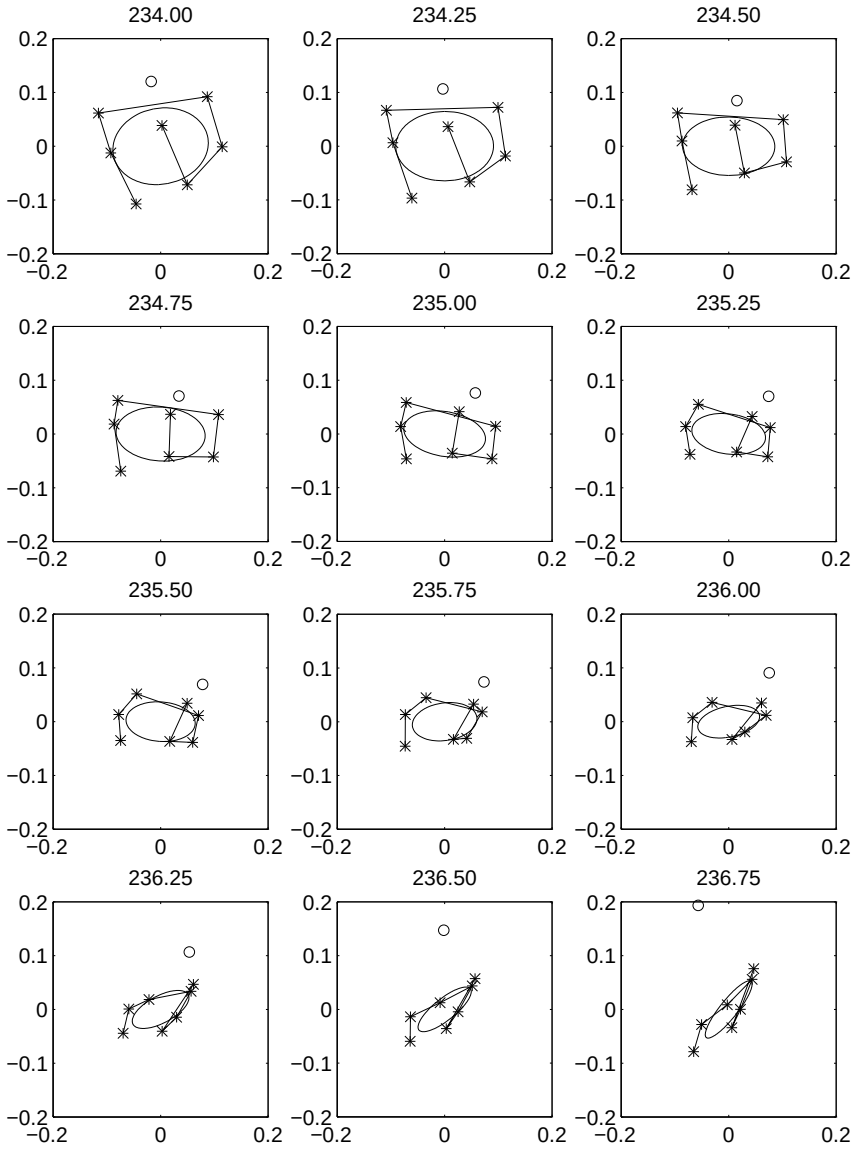

Figure 5.1: Time-sequence of drifter field at tip of perturbation. The interpolated locations of the drifters are indicated with the '$*$' symbol, with a single drifter not used in the area estimation indicated with a '$\circ$' symbol. The ellipses graphically represent the major and minor axes of displacement of the drifters. Data are interpolated to the time interval shown, and the drifter field is centered around the mean location of the field at each time step.

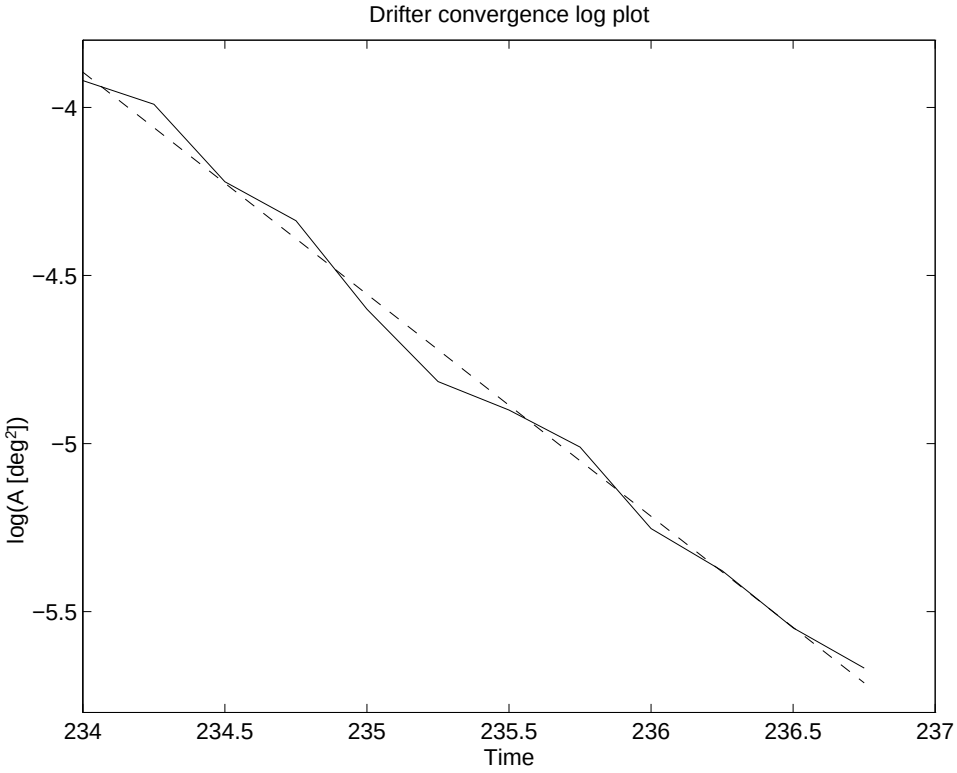

Figure 5.2: Time-series of the natural logarithm of the ellipse areas found in Figure 5.1. The solid line shows the actual area measurement and the dashed line shows a linear fit to this curve.

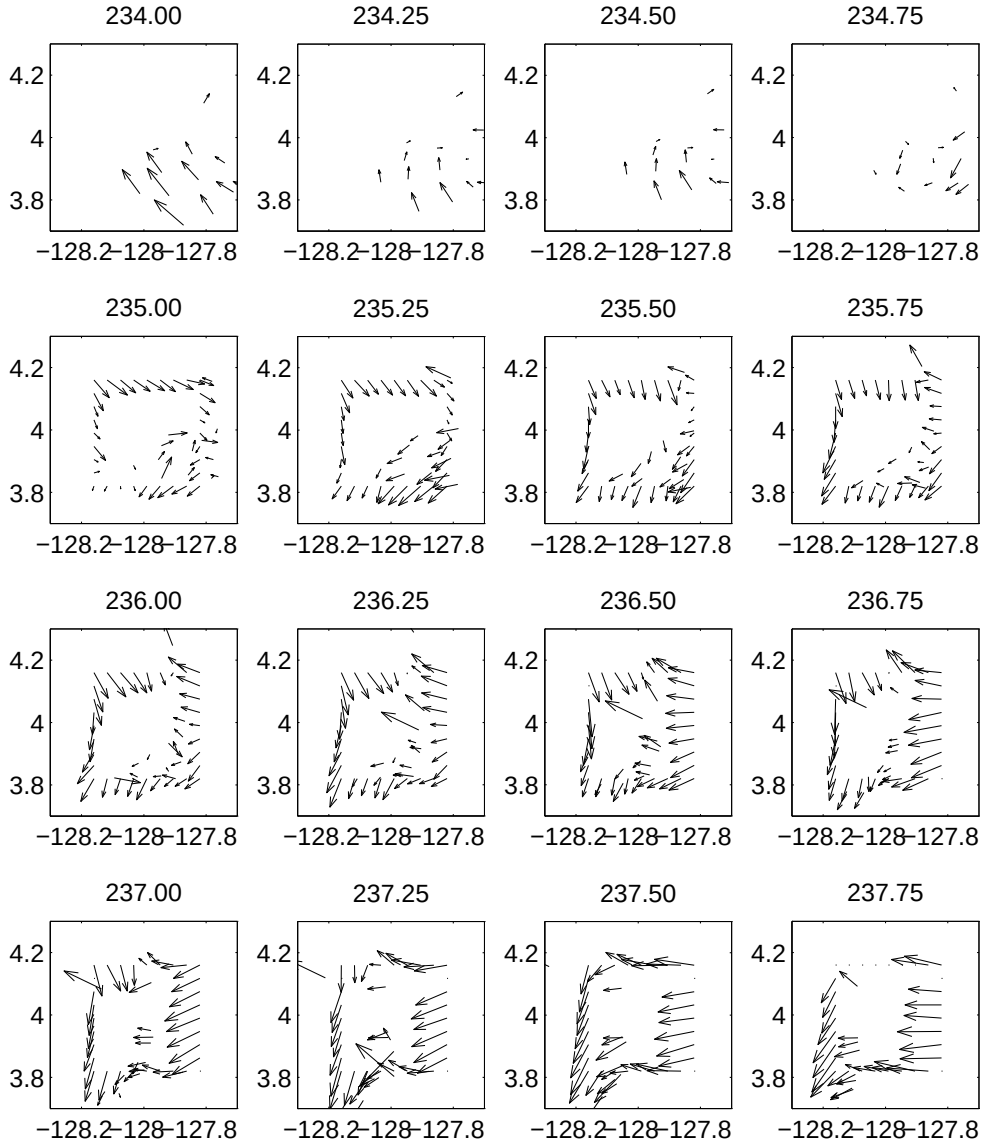

Figure 5.3: Velocity data from MW9010 box survey at the northern "tip" of the perturbation. Velocity data are taken from the motion of the drifter field and from the ADCP, and are interpolated to the same time grid as in Figure 5.1.

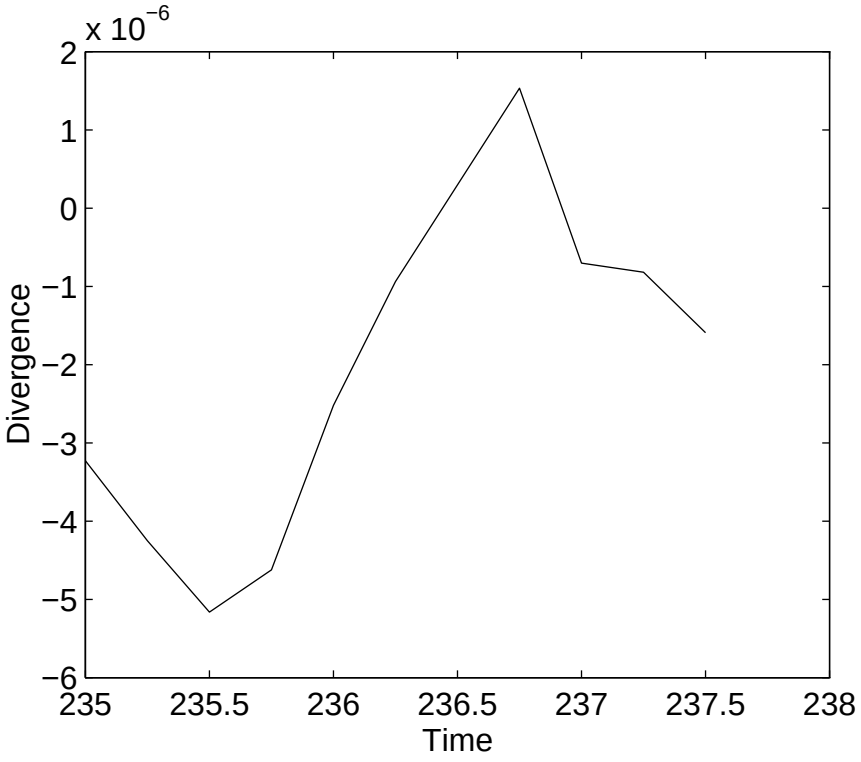

Figure 5.4: Divergence estimates from the MW9010 box surveys.

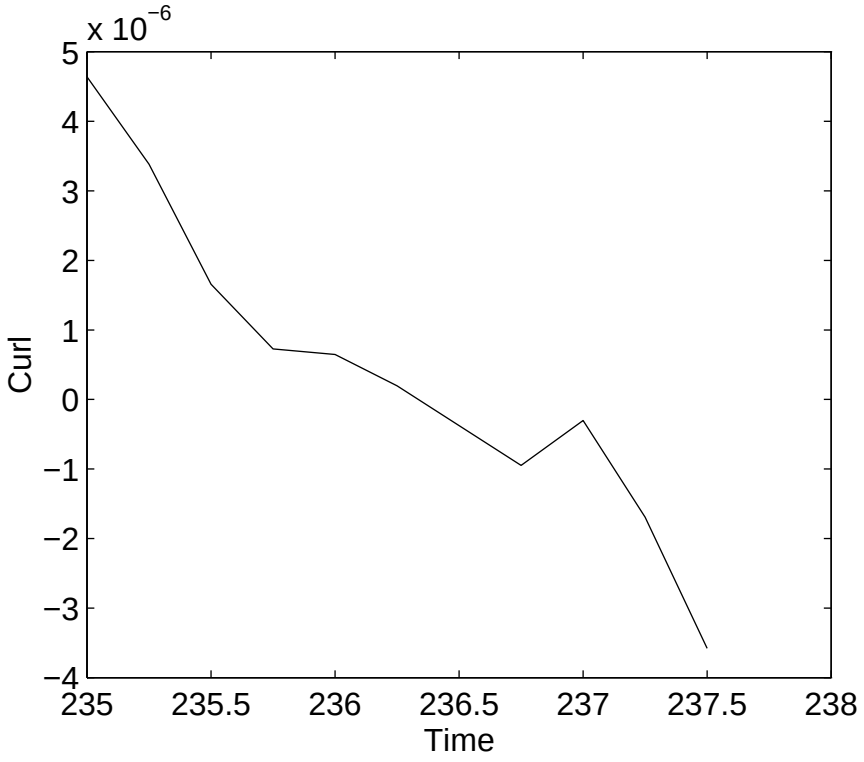

Figure 5.5: Vorticity estimates from the MW9010 box surveys.

Chapter 6

The Trailing Edge of the Wave

During MW9012, a section was conducted in the trailing edge of the perturbation, oblique to the nearly meridional front. CTD stations were conducted every 20 km along this section. The region of cold water was to the southwest of the front, warmer water to the northeast. In this chapter, the dynamics of this trailing edge of the perturbation will be examined.

6.1 Convergence and Subduction

Figure 6.1a shows the temperature field from this section and Figure 6.1b shows the zonal (across-front) velocity. As in the leading-edge crossing, the cold side of the front was well mixed thermally from the surface to the 150 dbar thermocline. On the warm side of the front, a well-mixed warm layer extended from the surface to around 50 dbar, capping a cold region from 50 dbar to the 150 dbar thermocline.

Divergence and vertical velocity derived from this section were clearly unrealistic (Figure 6.2); large vertical velocities crossing the 150 dbar thermocline which cannot exist in nature were found. Thus, an assumption of along-front invariance cannot be made in this area.

A region of strong eastward flow was seen at around 125 dbar to the west of the surface front. Because of the oblique angle between the front and the ship track, it is impossible to determine whether the sharp gradient of this flow was due to along-track or across-track variations.

6.2 Along-Front Jet

Figure 6.3b shows meridional velocity of this transect and Figure 6.3a shows the salinity field. A high salinity jet was observed moving toward the south just below the subduction thermocline, centered at around 110 dbar depth, 0.15° east of the surface front. The core of the jet had a velocity of in excess of 0.7 ms^{-1}, with a salinity of around 35.0. This jet extended to the west, flowing with a velocity of between 0.3 and 0.4 ms^{-1} between 100 dbar and the 150 dbar thermocline with a salinity in excess of 35.1. The water properties of this jet were similar to the high-salinity water observed both in the leading-edge front and the box survey to the north.

6.3 Comparison to Leading-Edge Crossing

While no quantitative analysis can be made of these data because we cannot separate between along-front and across-front changes, the basic picture of subduction from this crossing is similar to that of the leading-edge crossing: Cold equatorial upwelling water flowed toward the front and is subducted below a $50 \sim 75$ dbar thick layer of warmer water. A jet of high-salinity water moved along the front at a velocity of $0.7 \sim 0.8$ ms^{-1} in a generally eastward direction, following the front.

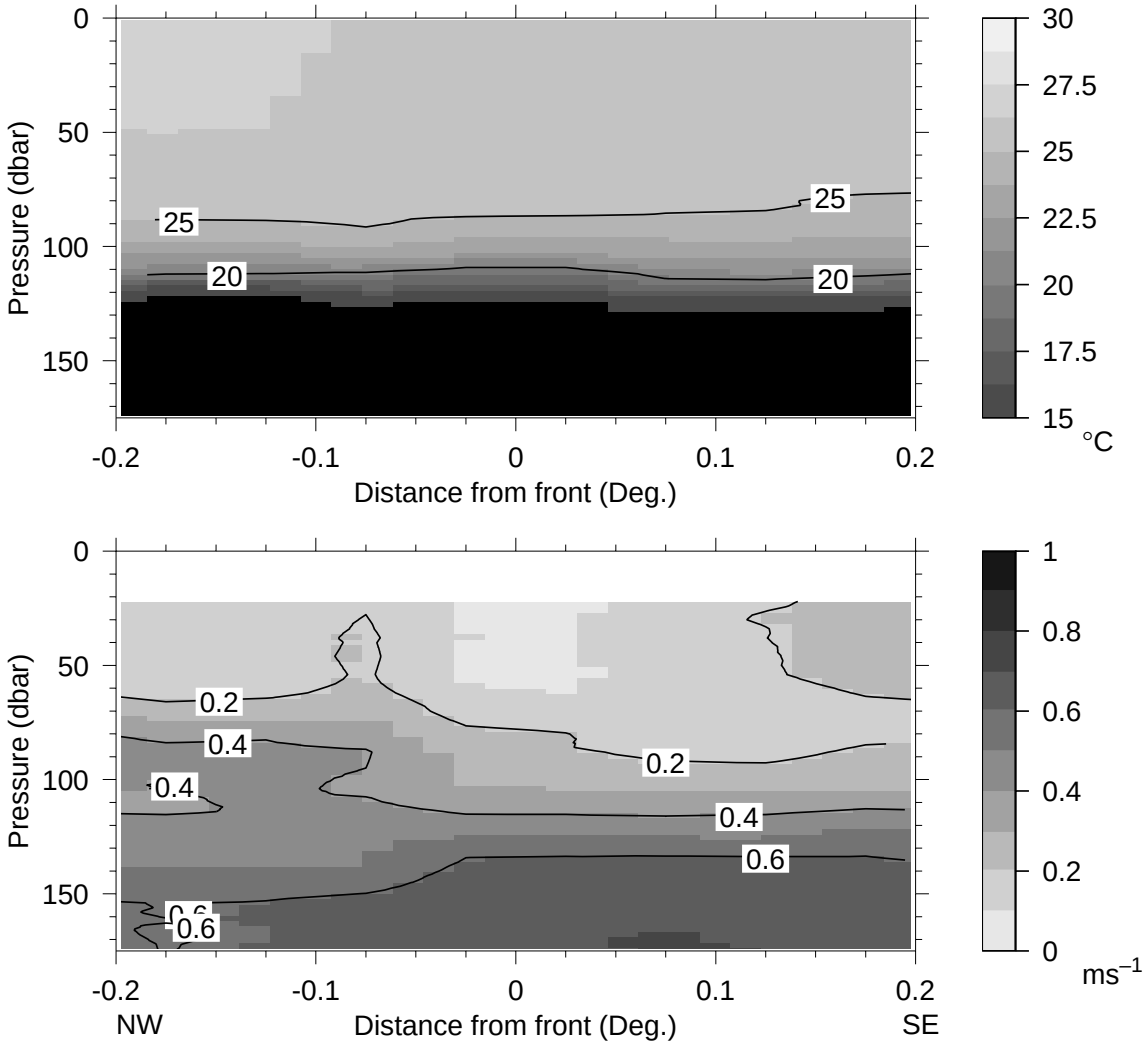

Figure 6.1: Temperature (upper panel) and across-front velocity (lower panel) of trailing edge front crossing. Temperature contours are shown every 5°C with grayscale changes every 1.25°C. Velocity contours are shown every 0.2ms^{-1} except at $0\ \text{ms}^{-1}$ with grayscale changes every 0.1ms^{-1}.

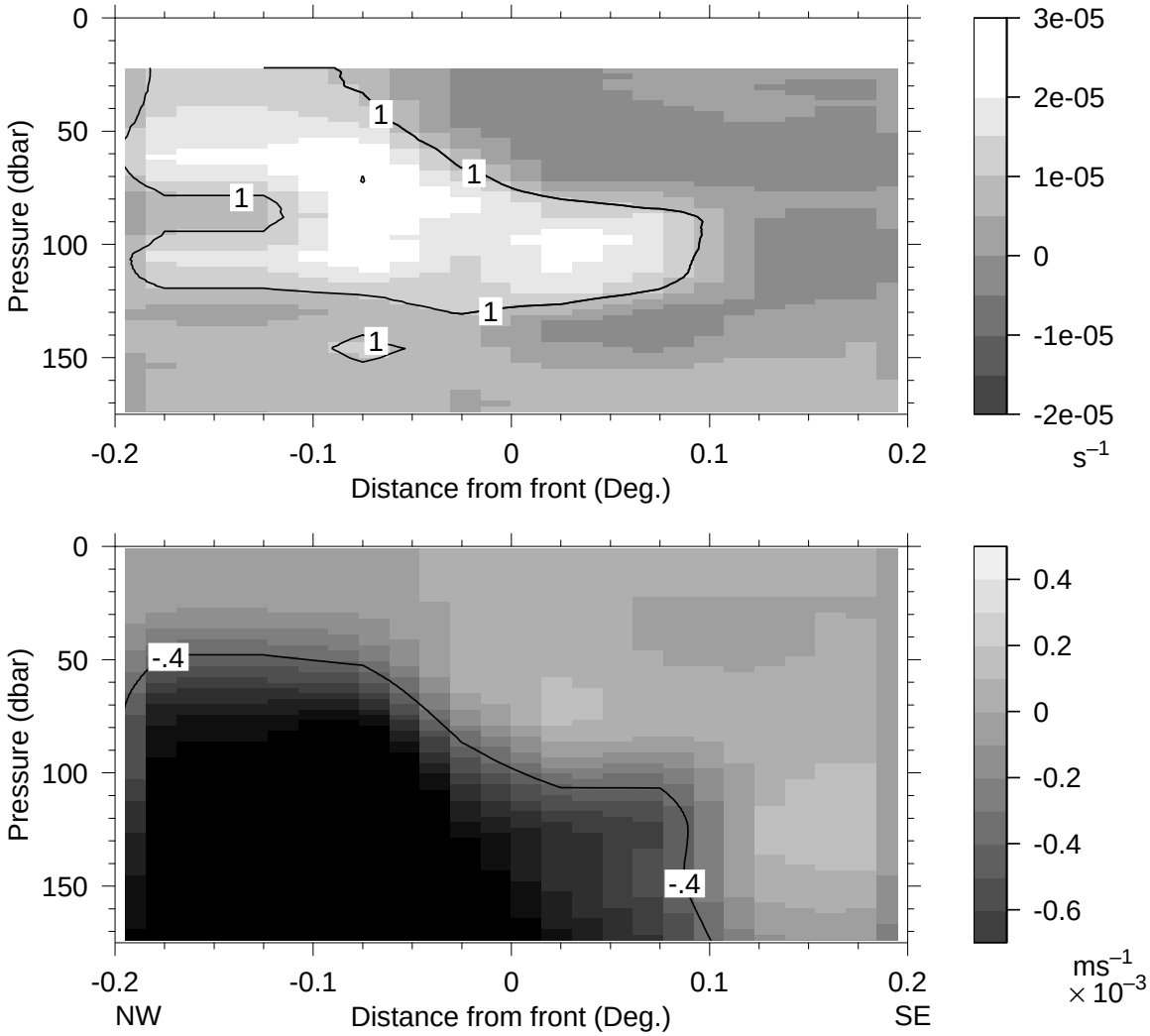

Figure 6.2: Divergence (upper panel) and vertical velocity (lower panel) of trailing edge front crossing. Divergence contours are shown every 2×10^{-5} sec^{-1} with grayscale changes every 0.5×10^{-5} sec^{-1}. Velocity contours are shown at $\pm 0.4 \times 10^{-3}$ ms^{-1} with grayscale changes every 0.1×10^{-3} ms^{-1}.

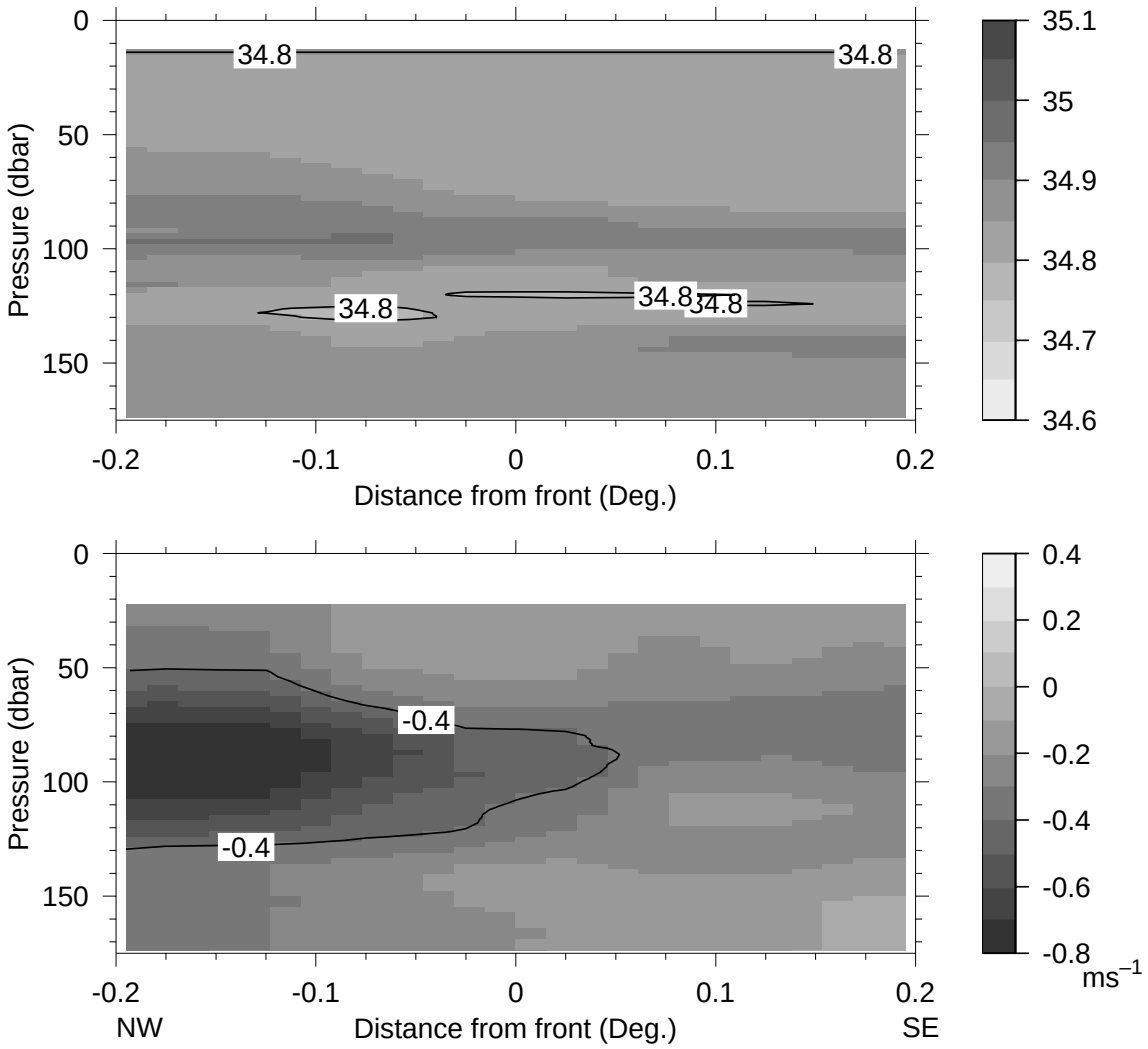

Figure 6.3: Salinity (upper panel) and along-front velocity (lower panel) of trailing edge front crossing. Salinity contours are shown every 0.2 with grayscale changes every 0.1. Velocity contours are shown at 0.4 ms^{-1} with grayscale changes every 0.1 ms^{-1}.

Chapter 7

The Along-Front Jet:Discussion

In all observations, a jet of high salinity was observed associated with the North Equatorial Front. This jet remained trapped along the front, transporting high salinity water across the equator and to the north. This jet will be discussed in this chapter.

7.1 Thermal Wind Relation

The u component of the thermal wind equation is given by [Gill, 1982]

$$f\frac{\partial u}{\partial p} = -\rho^{-2}\frac{\partial \rho}{\partial y}, \tag{7.1}$$

giving a relation between density gradients and current shear, where u is the along-front velocity in a frame of reference moving with the perturbation, and v is the across-front velocity in the moving frame. Because the frame of reference moves at a constant velocity, this does not affect the calculation in 7.1. Figure 7.1 shows a comparison of the vertical shear of along-front velocity predicted from thermal wind with that measured by the ADCP. The vertical shear along the base of the along-front jet was consistent in both fields, though was much stronger in the ADCP. This suggested that the jet approximately followed the thermal wind relation.

The shear along the subduction thermocline was not as well represented, suggesting that significant terms were neglected; in this region the frontal processes are significantly ageostrophic. Below the surface front, at 140 dbar, the thermocline shear was misrepresented: the shear predicted by thermal wind had the reverse sign as that measured by the ADCP.

Thus, although the subsurface jet appeared in geostrophic balance, other features

violated this approximation. Since the full three-dimensional field was not available, the additional terms could not be measured, thus a full momentum balance could not be produced.

7.2 Along-Front Vorticity Balance

The conservation of potential vorticity is given by

$$\frac{\mathrm{d}}{\mathrm{d}t}\left(\frac{\zeta + f}{h}\right) = 0. \tag{7.2}$$

Considering that the surface layer at the front is subducted and carried toward the northwest while thinning, a change in potential vorticity can be predicted from the above equations. $|\zeta|$ appears to be small in the upper layer east of the front, an estimate of vorticity ζ to the west of the front can be found under the assumption that the front is at a steady-state. Since h decreases and $f = \beta y$ increases, ζ must decrease.

(7.2) can be rewritten

$$\zeta = C\frac{\delta p}{\delta \rho} - \beta y, \tag{7.3}$$

where

$$C = \left(\frac{\beta y + \zeta}{\frac{\delta p}{\delta \rho}}\right)_{t_0}. \tag{7.4}$$

Figure 7.2 shows a comparison between the potential vorticity predicted from Equation 7.3 and that measured from the ADCP. The fields have some similarities. The change in vorticity associated with the along-front jet (denoted by the 1.2 contour in the figure) was observed in the predicted field, though much weaker than in the measured field. The region of high vorticity associated with the subduction thermocline was also observed in the predicted field.

Although there was some agreement between the two fields, significant differences were observed. These differences can be attributed to assumptions made in producing the fields. Equation 7.2 assumes that the tilting term is not significant in the vorticity balance, which may not be a safe assumption in the vicinity of a strong oceanic front. Furthermore, only the across-front gradient of along-front velocity is measured, assuming that the along-front gradient of across-front velocity is insignificant. While this may be true in the average, patchiness in the field would result in significant error in the measured vorticity. Further data is needed to construct a more reliable vorticity balance.

7.3 Mixing

The gradient Richardson Number (Ri) is defined as the ratio of the buoyance frequency and the vertical shear of horizontal velocity. Kundu [1990] and others show that for values of Ri greater than 0.25, linear stability is guaranteed. For values of Ri less than 0.25, instability is possible, but not guaranteed.

Figure 7.3 shows scatter plots of bouyancy frequency against vertical shear of horizontal velocity. The predicted cutoff at a Ri of 0.25 was clearly visible, although some measurements lay below this line. Figure 7.4 shows Ri over the frontal crossing section. The 150 dbar thermocline was stable with Ri approaching 10. Below the 150 dbar thermocline, the water column remained generally stable as well. The subduction thermocline was relatively stable, with Ri remaining above 3 over most of the region.

To the south of the front, Ri was close to 0.25, suggesting that mixing may have been occurring in this region. Within the jet below the subduction thermocline, similar values were seen, with a region of slightly increased Ri between the two areas. The warm surface trapped layer was not as well mixed; Richardson numbers varying from 0.25 to

5 were found within this region. Thus, mixing due to dynamic instability was not likely to play a significant role in either the along-front jet or the subduction thermocline.

7.4 Water Types

Figure 7.5 shows a temperature-salinity diagram representative of the frontal crossings. Four distinct regions are identified. The off-equatorial water, denoted ITCZ water since it was characteristic of conditions in the ITCZ, had a temperature in excess of 25.5°C and salinity around 34.9. The upwelled water had similar salinity to the ITCZ water, with temperatures around 25°C, mixing via two distinct paths to a salinity of 34.95 and temperature of 24.5°C. The along-front jet was visible as the high-salinity limit of the profile, with a salinity as high as 35.2 and temperature of 24.5°C. The curve toward cold, low salinity water represented the transition across the 150 dbar thermocline. Although the scatter of this curve suggests mixing over a number of water types, a large amount of mixing across the thermocline was observed in the region of the along-front jet water type.

Figure 7.6 shows three temperature-salinity diagrams from the leading edge crossing. To the northwest of the front (in the region where the warm ITCZ water was above the upwelled water), all regions defined above were identified. In both of these diagrams, the jet water had salinities reaching nearly 35.1 at a temperature of 24.0°C, and the primary mixing across the 150 dbar thermocline was between the upwelled water and the deep water.

However, just southeast of the front both the ITCZ water type and the jet water type were absent from the temperature-salinity diagram. This is expected; the front

serves as the boundary the ITCZ water cannot cross and the jet was observed trapped just northwest of the front.

Figure 7.7 shows a temperature-salinity diagram from 50 km east of the northern tip of the perturbation. This diagram was nearly identical to those observed to the northwest of the front in the leading-edge crossing. The jet water reached a salinity of nearly 35.1 with a temperature of around 24°C, as in the leading-edge crossings. Thus, the jet has maintained its identity to the point where it reaches the northern extent of the front.

Figure 7.8 shows a temperature-salinity diagram from the trailing-edge crossing. The ITCZ and upwelled water types are identifiable in this diagram, but the high-salinity core of the jet water was seen with a maximum salinity of 35.0.

Figure 7.9 shows a series of CTD stations conducted between two perturbations. Although an isolated high-salinity core was not observed, regions of high salinity with temperatures similar to those found in the jet are observed.

Figure 7.10 shows a section across the eddy associated with the perturbations of the North Equatorial Front. The high salinity cores around 100m at 140°W and 136°W were likely associated with this jet, smoothed out in producing the map of the eddy. Thus, this jet represents a northward transport of high-salinity water.

Figure 7.11 shows typical distributions of water at the $\sigma = 25\text{kg/m}^3$ ($\delta_t = 300$ cl/t) density surface. From these data, a gradient of salinity across the equator was seen, suggesting that salinity in excess of 35.0 is uncommon to the north of the equator while salinities below 35.0 are uncommon to the south. However, the jet water observed in the leading-edge crossing was well in excess of 35.0 and observed as far north of 5°N.

Figure 7.12 shows a conceptual diagram of the flow of the jet, as hypothesized from

these data. Along the equator, high salinity water is transported to the east in the EUC. The along-front jet closely matched the water characteristic of the EUC just south of the equator [Montgomery and Stroup, 1962], suggesting that it has its source in the EUC. Since salinities greater than 35.0 are seldom seen north of the equator [Tsuchiya, 1968], the origin of the water in the jet is likely south of the equator. At the northern tip of the perturbation, the jet detached from the front, gradually turning back to the south in the large-scale eddy associated with the perturbation, mixing with the surrounding water. As it crossed the North Equatorial Front along the trailing edge, its salinity was reduced by over 0.1, having mixed with water to the north. Thus, a net transport of salt to the north is seen.

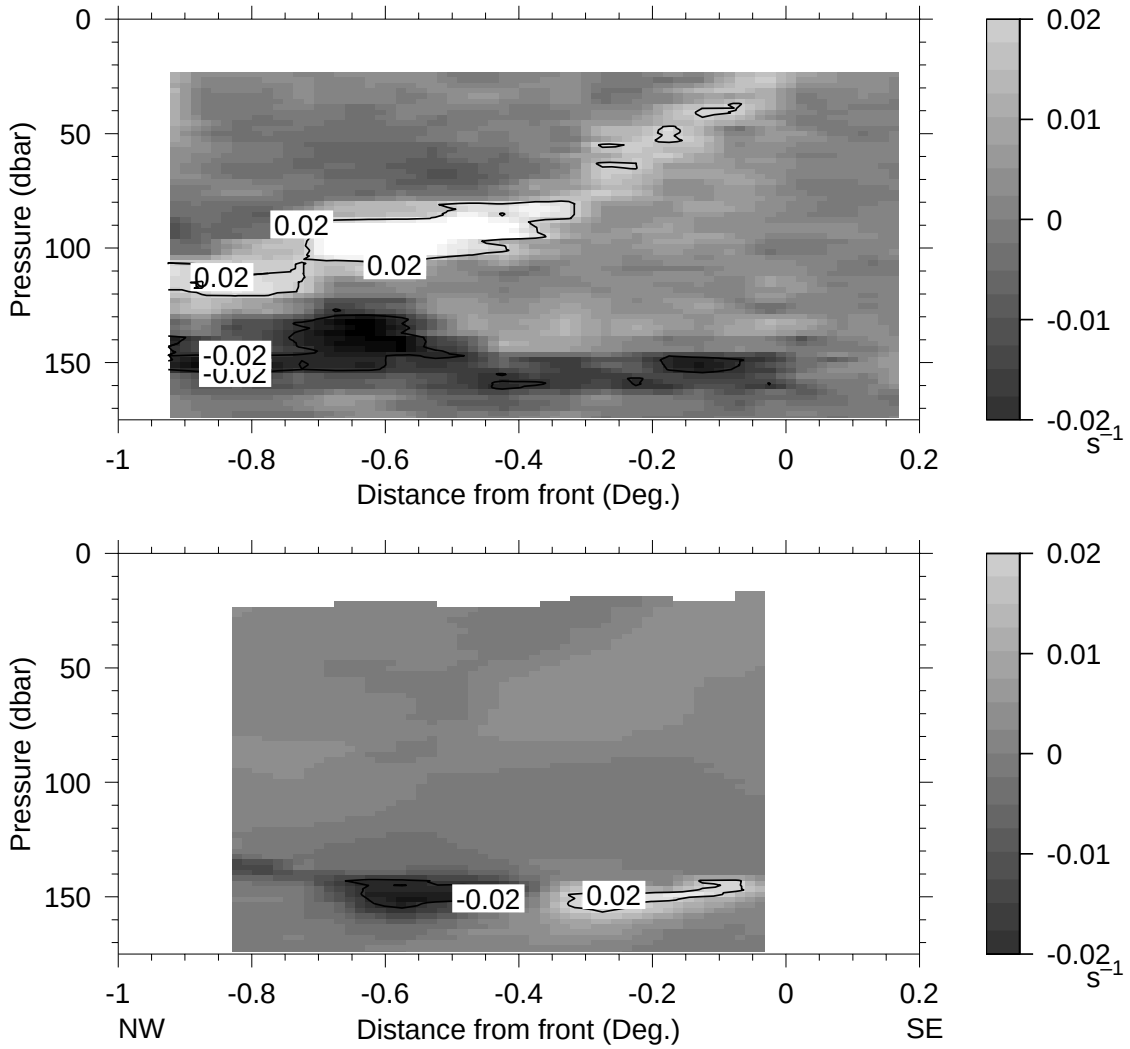

Figure 7.1: (a) Shear of along-front velocity as observed from ADCP data. (b) Shear of along-front velocity as predicted by geostrophic balance.

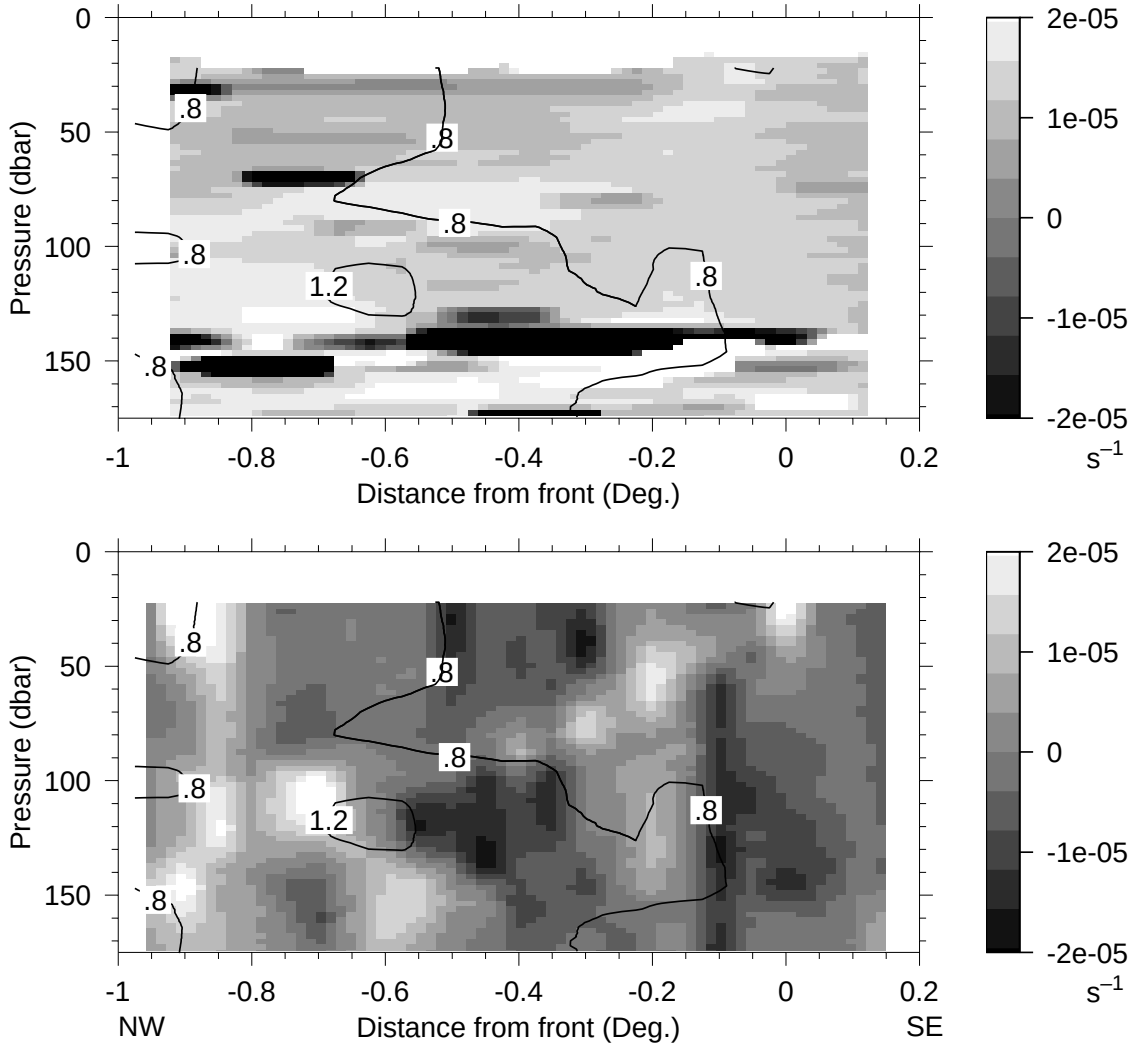

Figure 7.2: (a) Potential vorticity as predicted from conservation equations, as described in Section 7.2. (b) Potential vorticity, as measured from ADCP data. Both figures have ADCP along-front velocity overlayed.

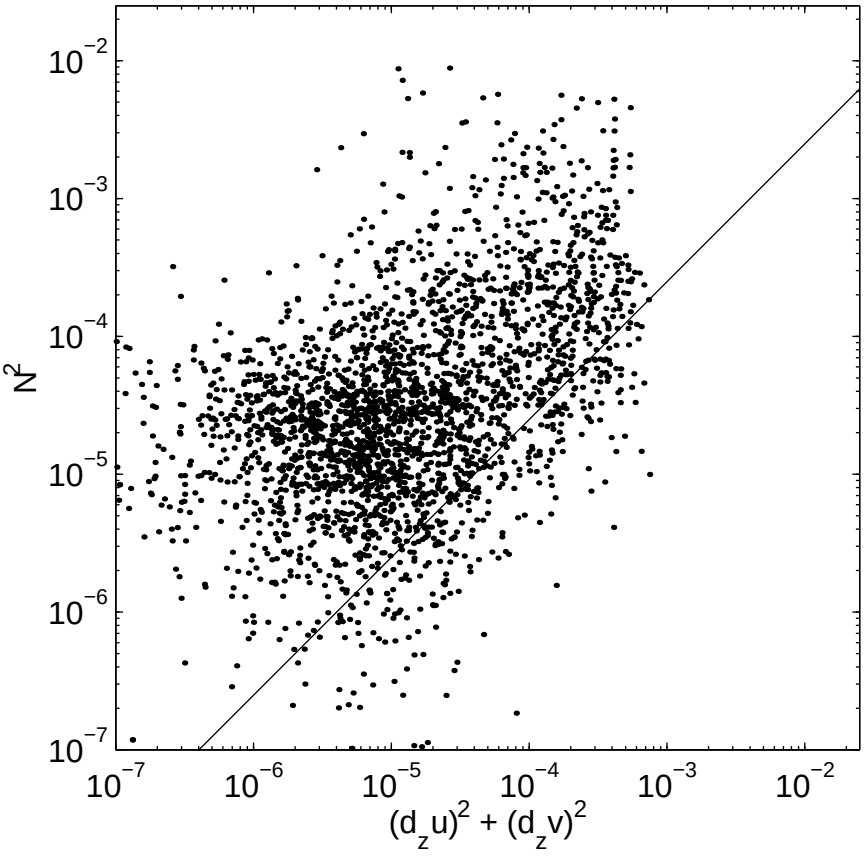

Figure 7.3: Scatter of N^2 and $\partial_z u^2 + \partial_z v^2$ from leading-edge crossing

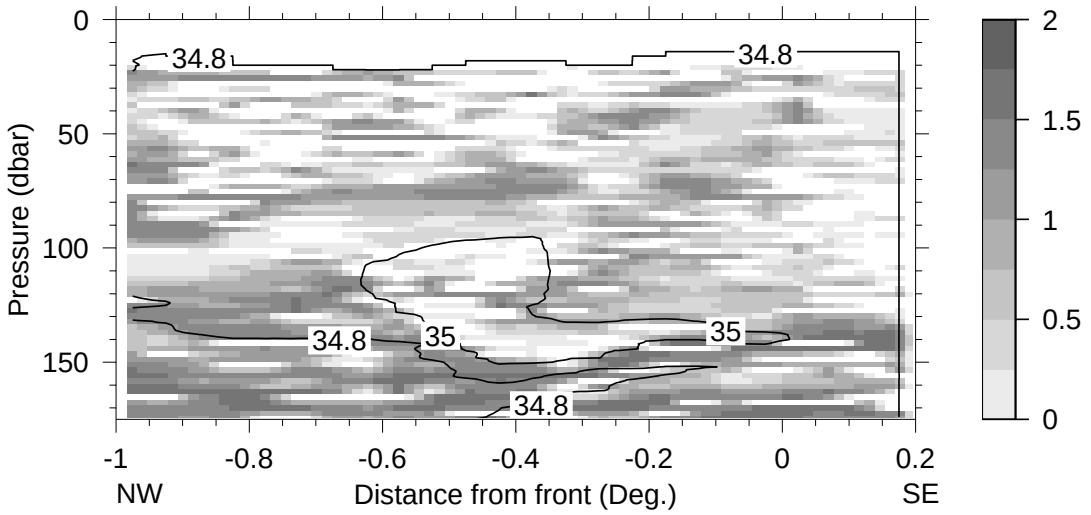

Figure 7.4: Richardson number field from leading-edge crossing.

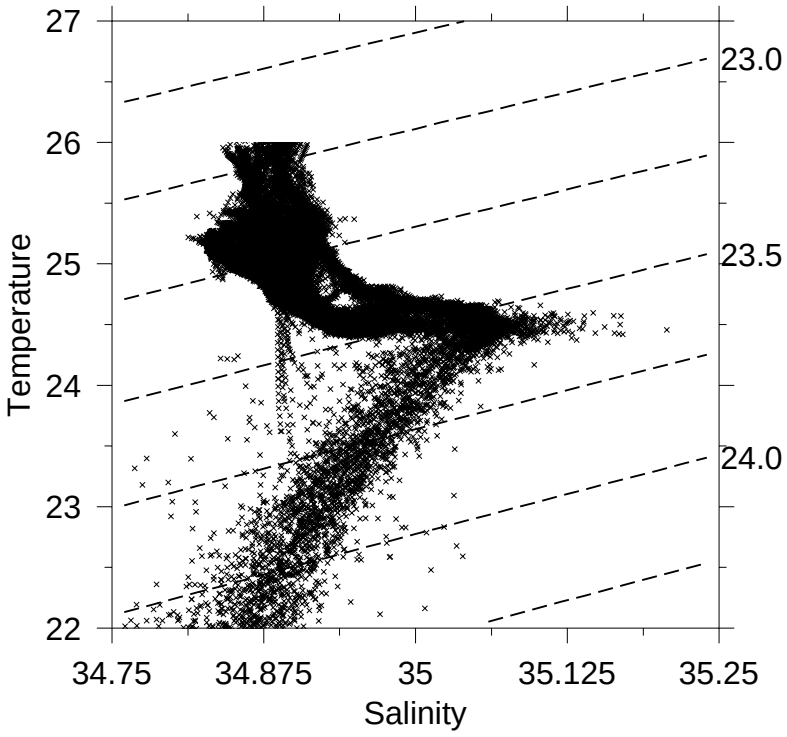

Figure 7.5: Temperature-salinity diagram representative of the frontal crossings. Isopycnals are shown on σ_t surfaces.

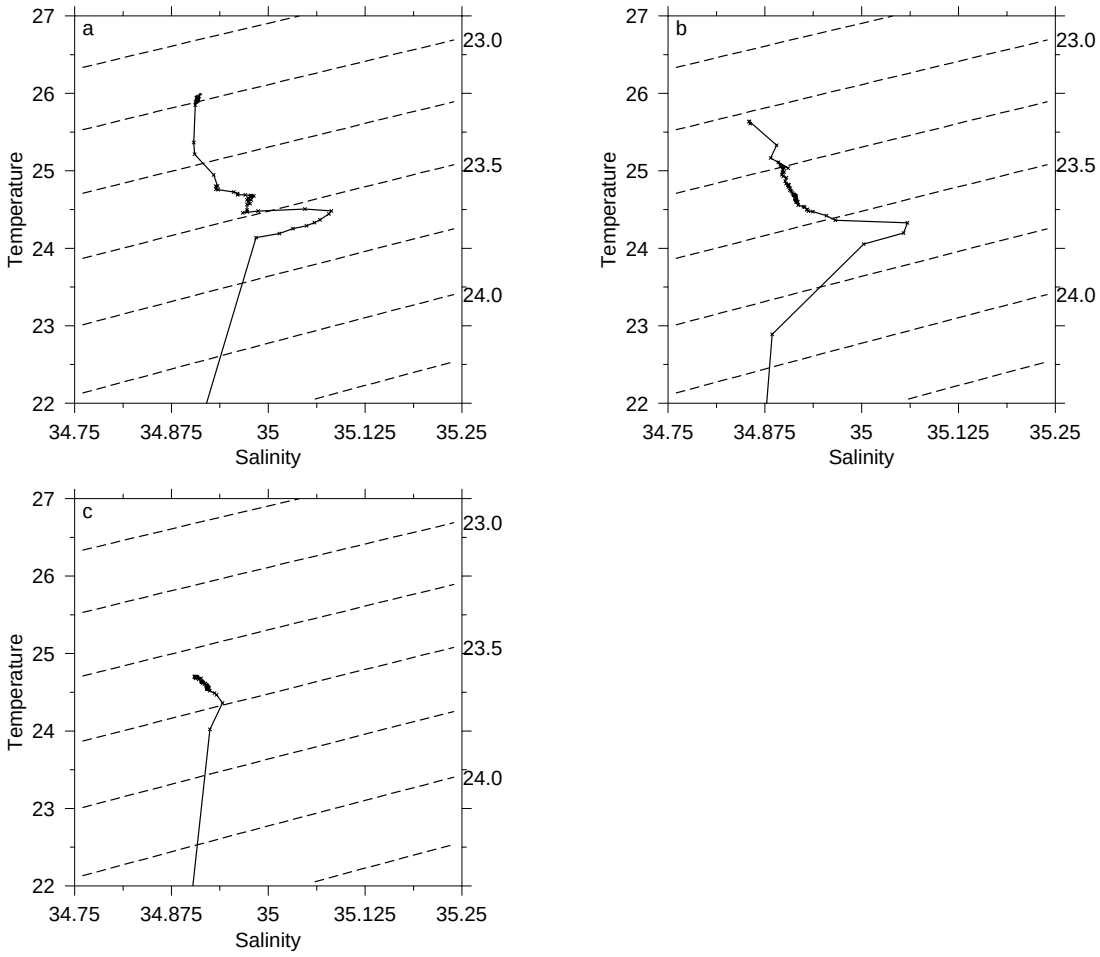

Figure 7.6: Temperature-Salinity diagrams of (a) 35km northwest of the front, (b) 3 km northwest of the front, and (c) 13 km southeast of the front, collected during the leading-edge crossing. Isopycnals are shown.

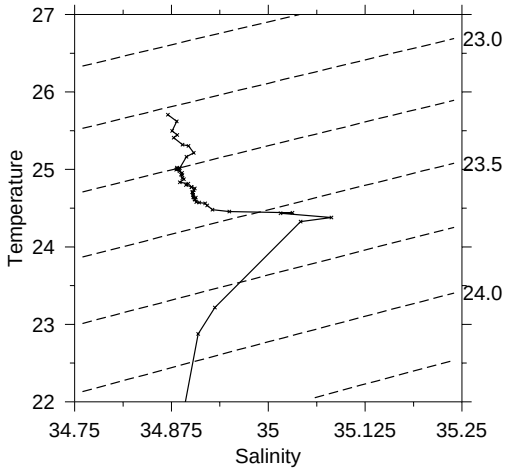

Figure 7.7: Temperature-Salinity diagram collected during the northern tip box survey. Isopycnals are shown.

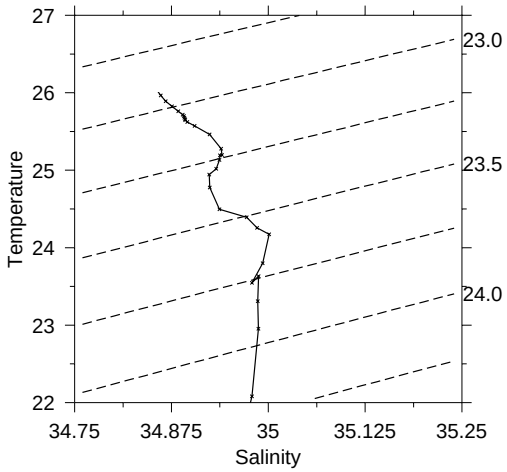

Figure 7.8: Temperature-Salinity diagram collected 35 km north of the trailing-edge front. Isopycnals are shown.

Figure 7.9: Series of CTD stations conducted between two perturbations of the North Equatorial Front.

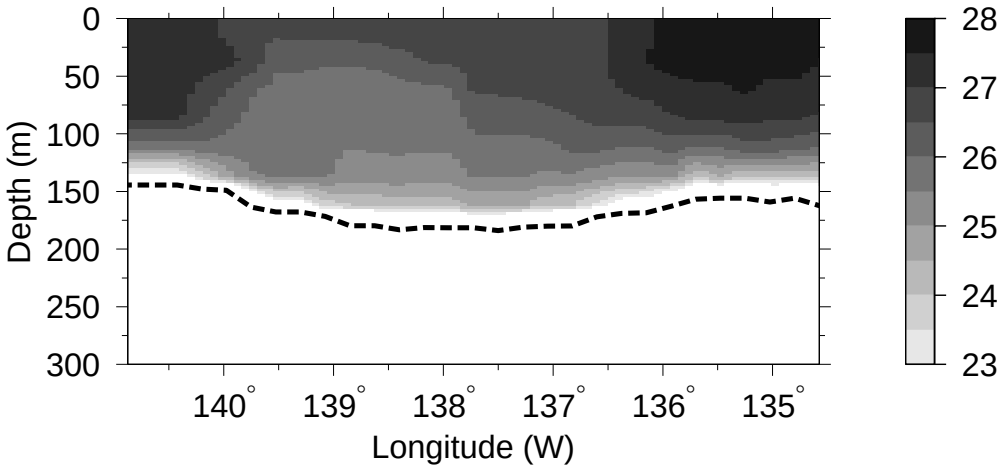

Figure 7.10: Temperature section across the eddy associated with the perturbations of the North Equatorial Front. The dotted line indicates the mixed-layer depth. *From Flament* et al *[1996].*

Figure 7.11: Typical water distributions of salinity at the 200 cl/t surface. *From Tsuchiya [1968].*

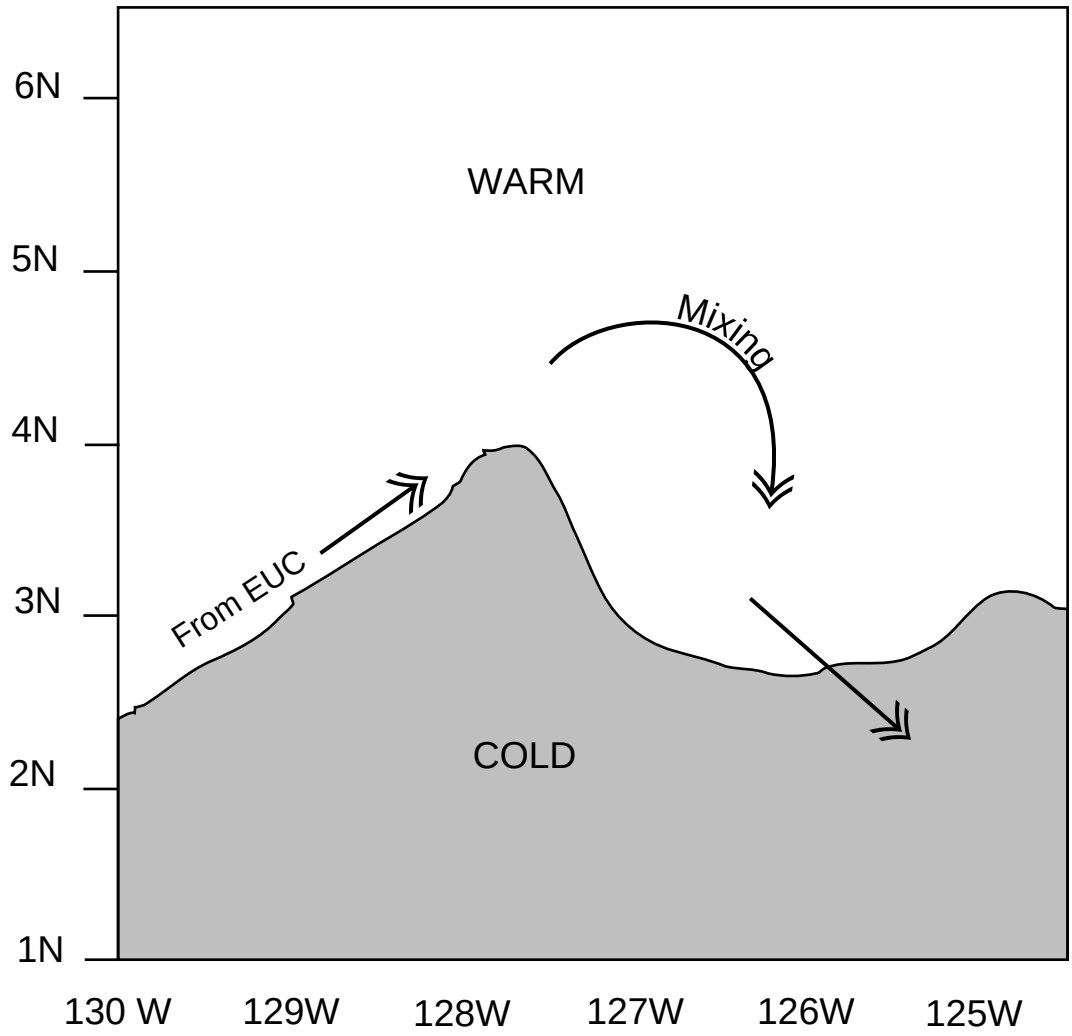

Figure 7.12: Schematic representation of high-salinity jet.

Chapter 8

Summary

8.1 Large-scale dynamics

The shear between the NECC and NEC played a direct role in the evolution of perturbations in the North Equatorial Front; in MW9010 and JGOFS it produced a modulation of the amplitude of the perturbations through a meridional dependence in phase speed. During MW9012, an eddy was observed in association with the frontal perturbations which showed reduced temporal variability from MW9010. The difference between MW9010 and MW9012 was not inter-seasonal; MW9010 and MW9012 were performed during the same instability wave season separated by less than two months. However, during MW9012, the equatorial upwelling was strengthened and had time to reach a state of equilibrium and establish the observed eddy motions.

Thus, a basic picture of the intra-seasonal variations in the North Equatorial Front can be seen. As the trade-wind system strengthens, equatorial upwelling increases, forming the cold tongue. The upwelled water begins to flow away from the equator, meeting the warmer surrounding waters to the north and south. Where the two water masses meet, a sharp front is created, on which regular perturbations form. As the shear between the NEC and NECC increases with increasing trade winds, the structure of the perturbations is sheared, resulting initially in a modulation in the amplitude of the perturbations. Later, either due to further increasing current shear or sufficient time to reach equilibrium, the structure of the perturbation stabilizes, carrying cold water away from the equator in periodic "plumes" associated with a traveling eddy.

8.2 Convergence and Subduction

From these observations, a picture of the basic frontal dynamics is formed: The cold equatorial upwelling waters move toward the northwest, where they encounter the warmer ITCZ waters. There is strong convergence along the front between the two water masses and the cold water is subducted below the warm layer. The primary 150 dbar thermocline is only slightly disturbed by this process, and an intermediate subduction thermocline is formed between the two water masses at around 75 dbar.

This view of the dynamics of the front is consistent with other observations of oceanic fronts. Eriksen, *et al.* [1991] shows a similar situation in the subtropical Atlantic, with a warm layer capping subduction of cold water along an oceanic front. Johnson [1996] shows detailed hydrographic data from the JGOFS experiment, indicating a similar subduction layer.

Rates of surface convergence of 5×10^{-5} were found from these data, giving a maximum downwelling velocity of around 0.008 ms^{-1}. These values are consistent with Johnson's findings of a maximum convergence of $4 \times 10^{-5} s^{-1}$ and a maximum downwelling velocity of 0.008 ms^{-1}. The assumption of along-front homogeneity is also supported by Johnson's findings; along-front convergence rates were more than an order of magnitude lower than across-front.

Because of the strong surface convergence, any surface trapped material in the water will tend to concentrate along the front, including plankton capable of regulating their depth. In addition, the equatorial upwelling waters carry a large nutrient load, making the fronts regions of high productivity in a region otherwise noted for low productivity values [Yoder *et al.*, 1994].

8.3 Along-Front Jet

A strong jet of high salinity water associated with the North Equatorial Front was observed at all frontal crossings, located between around 75 dbar and 100 dbar, moving toward the north at the leading edge of the front, returning to the south in the trailing edge. This jet was characterized by a temperature of around 24.5°C and a salinity of around 35.1 at the leading edge, reduced to around 35.0 at the trailing edge. Because of the high rain input in the ITCZ, there is a distinct salinity gradient in the equatorial Pacific with higher salinity water to the south. CTD stations closer to the equator during MW9010 show the 35.1 salinity water falling between the equator and 1°N. No station conducted north of 1°30′N, except those in the vicinity of the North Equatorial Front, showed salinity in excess of 35.04, although some stations showed narrow (20 dbar) regions of salinity around 35.0 just above the 150 dbar thermocline.

8.4 Future Work

This thesis has presented a basic overview of the subduction and convergence associated with the North Equatorial Front and a description of a high-salinity jet running along the front, representing a net transport of salinity to the north. However, much of the research was conducted using a single crossing of the front, with the assumption that this is representative of a "typical" perturbation in the North Equatorial Front.

Recent satellite data from the Earth Resource Satellite-1 (ERS1) Scatterometer as well as from the Shuttle Radar Laboratory (SRL) project are available over the TIWE study region, and clearly show the perturbations in the North Equatorial Front. Winds measured from the scatterometer will be compared to *in situ* wind measurements

during MW9010 and MW9012 to determine differences in atmospheric forcing between the situation in 1990 and other instability wave seasons. In addition, because the SRL radar has sufficient resolution to resolve surface swell, retraction by changes in surface current will be investigated using these data.

Appendix A

SeaSoar data processing

A.1 Introduction

One of the objectives of the *R/V Moana Wave* cruises 9010 and 9012 was to study the variations of temperature, salinity and density in response to the passage of instability waves near 140°W, in the framework of the Tropical Instability Wave Experiment. During the first cruise (TIWE-1), a zonal section along $\sim 3°$N from 145°W to 126°W was sampled twice, separated by an intensive frontal survey near the eastern-most point. In the second cruise (TIWE-2), a box $\sim 1.5° \times 3°$ centered on 140°W 3°25′N was sampled six times over the period of an instability wave. In addition to the tropical legs, a shakedown period at the start of the first cruise (HaRP-1), as well as a few days remaining in the ship schedule at the end of each cruise (HaRP-2 and HaRP-3) were used to study the response of the ocean to wind stress variations in the lee of Hawaii, in the framework of the Hawaii Rainband Project. Data collected in both geographical areas are presented here. Dates and areas are given in Table A.1. Figure A.1 shows the areas of the TIWE cruises.

Hydrographic data were collected by two means on these cruises: conventional on-station conductivity, temperature, and depth (CTD) profiles to a depth of 300 m, and with a undulating towed CTD, the SeaSoar, manufactured by Chelsea instruments and loaned by Woods Hole Oceanographic Institution. This report presents the data from the SeaSoar CTD. Data from the conventional stations were presented by Trefois, *et al.*[1993].

Table A.1: Dates and areas covered by the cruises.

cruise	leg	dates	areas	
MW9010	HaRP-1	08/05 to 08/06	156°07′W	20°00′N
	TIWE-1	08/17 to 09/03	126°20′W to 145°40′W	1°10′N to 10°00′N
	HaRP-2	09/06 to 09/08	155°30′W to 156°20′W	18°30′N to 20°10′N
MW9012	TIWE-2	11/14 to 12/05	139°15′W to 140°45′W	2°05′N to 4°45′N
	HaRP-3	12/10 to 12/12	155°50′W to 158°00′W	18°24′N to 20°24′N

A.2 Towed Platform

The dates of SeaSoar deployments are found in Table A.2. The system was towed at about 8 kn on a 1000 m partially faired cable [Chelsea Instruments, 1987]. The angle of attack of the wings was controlled using a feedback loop from a pressure sensor in the SeaSoar. A complete undulation cycle took about 15 minutes. Since it was difficult to properly adjust the feedback loop to drive the SeaSoar to the desired depth, occasional data gaps were noted. In addition, during the downward motion, small undulations ("hiccoughs") in the depth were regularly observed, as seen in Figure A.2.

The SeaSoar was provided with two hydraulic units: serial number 008, installed in the vehicle, and serial number 010, provided as a spare. These units were constructed differently: the body of unit 008 was made of gray PVC whereas the body of unit 010 was stainless steel. During MW9010, unit 008 was deployed three times for a total of 77.5 hours before it failed. During the last 24 hours of operation, control of the SeaSoar became increasingly difficult, until the vehicle refused entirely to dive. Inspection of

Table A.2: SeaSoar deployments.

cruise	leg	dates	hydraulic unit	time
MW9010	HaRP-1	08/05 19:15 to 08/06 02:45	008	7:30
	HaRP-1	08/07 23:00 to 08/08 01:30	008	2:30
	TIWE-1	08/15 01:30 to 08/17 21:00	008	67:30
			Total for unit 008:	77:30
	TIWE-1	08/19 01:30 to 08/19 04:00	010	2:30
	TIWE-1	08/19 08:00 to 08/21 08:00	010	48:00
	TIWE-1	08/22 04:45 to 08/26 08:00	010	99:15
	HaRP-2	09/08 21:15 to 09/09 03:30	010	6:15
			Total for unit 010:	155:00
MW9012	TIWE-2	11/20 18:45 to 11/21 07:30	010	12:45
	TIWE-2	11/24 17:00 to 11/26 09:00	010	40:00
			Total for unit 010:	52:45

the SeaSoar revealed no foreign objects caught in the vehicle, and the on-deck response of the wings to the commands seemed normal. There was no obvious oil leak in the SeaSoar body and the oil levels seemed normal within the hydraulic unit. Lacking repair instructions and technical drawings, unit 008 was replaced with the spare, unit 010.

Since unit 010 was shipped dry, both internal oil volumes were filled with filtered oil, exercising the piston to expel any trapped air. The impeller section of the unit was found to be rotated 180 degrees compared to unit 008. Since the shaft was off-center, the propeller shroud fitted to the vehicle had to be removed to install the hydraulic unit.

Once deployed, the control signals operated in the reverse sense from normal: a "dive" signal caused the SeaSoar to rise to the surface and a "surface" signal caused it to dive. Reversing the polarity of the output from the deck unit corrected this problem. The SeaSoar was retrieved after 48 hours to allow deployment of drifting buoys.

It was then redeployed and functioned normally for about 99 hours, after which time it showed signs of fatigue and an erratic response, eventually refusing to dive. When retrieved, no foreign objects were on the cable or vehicle, and connections within the unit appeared normal. A 6 hour deployment was made at the end of the cruise near the Hawaiian islands, after which no further deployment of the SeaSoar was made.

Both units were sent back to Chelsea in October, where they were disassembled and cleaned. For unit 008, the internal oil volumes were found full and uncontaminated. Both electrical connectors were replaced. The failure of the unit during MW9010 was attributed to an electrical leak at a ruptured bulkhead connector, intermittently short circuiting the signal to the hydraulic valve.

For unit 010, the forward oil volume was full of sea water and a slight contamination

was found in the hydraulic circuit. The rubber bellow had detached from its seat on the piston shaft, creating a large oil leak. The failure of this unit was attributed to electrical leakage between two through-hull underwater connectors due to salt-water contamination of the hydraulic oil.

The refurbished units were shipped back to Hawaii for the second cruise in November. The presence of drifting fishing apparatus in the vicinity delayed the use of the SeaSoar, which was fitted with hydraulic unit 010. The SeaSoar was initially deployed for only 12.75 hours, followed by a deployment of 40 hours at the end of which the unit abruptly failed, refusing to obey commands from the deck unit. It was retrieved and hydraulic unit 010 removed.

The unit performed normally on the bench. There was no sign of oil leakage, both through-hull connectors were in good shape, and the oil levels were normal. This failure was attributed to an intermittent leak at the water-tight connections to the hydraulic unit, which were close to the rubber bellow and could easily have been pushed out or sideways as the bellow expanded and contracted.

During reassembly of hydraulic unit 008 at Chelsea, the hexagonal nuts that hold the front assembly to the PVC body had apparently been over-tightened, resulting in white cracks visible on the outside surface of the body, which were not present during the first cruise. Because the SeaSoar lacks a steel member between the instrument bay and the tail, the hydraulic unit has a structural function, making unit 008 unsuitable for deployment.

Due to the problems with unit 010 and the potential problems with unit 008, it was decided to terminate any further SeaSoar operations for the remainder of the cruise.

A.3 Sensors

The SeaSoar carried a SeaBird 9-11 CTD system fitted with two temperature sensors (model SBE-3, serial numbers 960 and 963), two conductivity sensors (model SBE-4, serial numbers 515 and 607) , a 3000 psi Paroscientific internal pressure sensor (model SBE-12, serial number 33729), a SeaTech stimulated fluorescence sensor, and, during MW9010 only, a dissolved oxygen sensor.

During MW9010, the sensors were mounted as shown in Figure A.3. The primary temperature and salinity sensors were mounted externally just forward of the fluorescence sensor. There was no pump used in this configuration, thus the sensors relied on the natural flow of water to remain flushed. The dissolved oxygen, secondary temperature, and secondary salinity sensors were mounted inside the body of the SeaSoar. During MW9012, the secondary temperature and conductivity sensors were mounted externally just behind the primary sensors, with only the fluorescence sensor mounted internally.

Internally mounted sensors were connected to an orifice at the front of the SeaSoar with a length of rubber tubing. Since this arrangement did not provide sufficient water flow, data from these sensors have not been processed.

Due to a configuration error in the SeaBird software, data from the fluorometer were not properly recorded, and were unavailable for additional processing.

A.4 Data Logging

A PC running SEASOFT version 3.4 controlled the CTD deck unit and provided logging and real-time display of data. In addition, the raw hexadecimal CTD data were recorded

and time-stamped on a Sun 4/20 connected to the deck unit's RS-232 port. The primary conductivity time-series was advanced by one sample (at 24 Hz). During MW9010, data were decimated to 12 Hz in the deck unit. During MW9012, all data were recorded at the full 24 Hz data rate, with no decimation.

The files from the Sun workstation were used as the primary source, with the PC files as a backup source. The frame counter provided by the CTD system was used to identify gaps in the data.

When a gap was found in the Sun file, the PC file was searched for the missing data. If the missing block was located in the PC file, it was inserted in the Sun file. Using this method all but a small number of gaps were filled. The remaining gaps were due to a loss of both data streams, possibly caused by a temporary communications problem between the underwater unit and the deck unit.

The MW9010 data were linearly interpolated to 24 Hz before processing since they were recorded at 12 Hz instead of 24 Hz.

A.5 Processing

An adaptive filtering technique was attempted to account for the variable response times of the sensors, using an optimal FIR filter design. Assuming that the responses of the temperature and conductivity sensors could be approximated by unknown FIR filters f and g respectively, a least-squares problem minimizing salinity spiking was cast to estimate these filters. Application of this technique yielded inadequate results. Since there was no pumping of the conductivity cells, their response functions varied over the duration of each profile. If the number of samples to consider when applying the least-squares analysis was chosen sufficiently small to follow the variations during a single

profile, there were insufficient data to assure a well conditioned covariance matrix, and a stable solution could not be found.

To determine the variations of flushing rate, the time series were divided into 128-sample segments, the squared fourier transforms of which were accumulated into one of eight bins, based on the pressures (p) and climb or descent rates ($\dot{p}$) shown in Table A.3. These bins were selected as classes in which the response of the sensors should remain approximately constant, allowing classical spectral analysis to be performed within each class.

Table A.3: Classes used in sensor alignment.

Class	$\dot{p}$(dbar/s)	p(dbar)	
1	$(-\infty, -2.5)$		Downcast, fast descent
2	$(-2.5, -1.5)$		Downcast, medium descent
3	$(-1.5, -0.5)$		Downcast, slow descent
4	$(-0.5, 0.5)$	$(0, 50)$	Stable, near surface
5	$(-0.5, 0.5)$	$(50, 250)$	Stable, middle depth
6	$(-0.5, 0.5)$	$(250, 400)$	Stable at depth
7	$(0.5, 1.5)$		Upcast, slow ascent
8	$(1.5, \infty)$		Upcast, fast ascent

A "modeled conductivity" M was derived from the measured temperature T as the conductivity required to produce a constant salinity of 34.5. Since conductivity is a weak function of salinity, the error introduced by this method is small. Power spectra of C and M from the primary sensors and their cross-spectra were averaged for each class. Figures A.4 and A.5 show the transfer function from C to M for each of the eight

classes.

The classes representing downcasts (1, 2, and 3) closely match on all days depicted. In addition, the mid-depth, stable case (class 5), matched the downcasts well (this condition only occurred during the "hiccoughs" encountered in the downcasts). Class 1 data also exhibited significant noise, and were not used for estimating the conductivity lag. For each of these classes, the transfer function magnitude was nearly unity to 2 Hz. A linear relation between frequency and transfer function phase was observed (Figure A.5), suggesting that delaying conductivity by $\sim 5 \times 10^{-2}$ seconds (slightly more than one sample) would produce a nearly uniform zero phase lag to approximately 2 Hz.

During the upcasts, it is suspected that eddies were shed in the wake of the SeaSoar body. These eddies may have induced dynamical pressure fluctuations, changing the flow rates through the sensors, which were not pumped. For classes 7 and 8, representing the upcasts, the transfer function magnitude remained near unity, although the phase was poorly behaved, especially in class 8. During the shallow and deep stable cases (classes 4 and 6), both the transfer function phase and magnitude showed erratic behavior. The shallow case (class 4) was particularly erratic due to trapped air bubbles near the surface. For these reasons, the upcast and stable data were not used in further processing.

A constant delay could not be applied to entire sections. To account for this change, the estimated delays averaged from classes 2, 3, and 5 were calculated hourly by linear regression to the averaged transfer function phase to 2 Hz. The median delays for each deployment are indicated on Figure A.6 (TIWE-2 was considered as a single deployment). Within each deployment, the delays were well centered around the median with no temporal trend, although, during MW9010, a long-term trend was observed over the

duration of the cruise. Changes in current shear when crossing a front, adjustments to the steering controls, and wear on the hydraulic unit also may have affected the angle of attack of the SeaSoar, thus changing the flow through the sensors.

The sudden jumps in delays shown in Figure A.6 were suggestive of unrecorded changes in the deck unit configuration. Regardless of the cause of the shifts, the delays shown were applied to the conductivity series as recorded, producing nearly zero transfer function phase. No further filtering of the time-series was performed.

The data was then calibrated as described in the following section, filtered using a 4 second running median, and decimated to 1 sample per second. The 1-second data were gridded on a 2 dbar $\times$ 5 minute grid by linear interpolation first along the pressure axis and then along the time axis between successive downcasts. When successive downcasts were separated by more than 30 minutes, no interpolation was performed.

A.6 Calibration

The sensors were calibrated by Sea-Bird Electronics in April, 1989, and a post-cruise calibration was performed in July, 1992. There were no conventional CTD casts within 12 hours of SeaSoar deployments, preventing direct comparison between the SeaSoar CTD and the conventional CTD. The only cross-calibrations possible were between the primary and secondary temperature and conductivity sensors. In the following cross-calibrations, only the downcast data as described in section A.5 were used. The secondary conductivity sensor, which was damaged between cruises, was repaired and recalibrated prior to the start of MW9012.

Comparisons between the primary and secondary sensors were obtained for MW9012, when secondary sensors were mounted externally. Because the secondary sensors were

mounted behind the primary sensors, the lag between them resulted in larger differences in the thermocline. Data were extracted from the gridded profiles at the surface and at 250 dbar pressure to avoid the thermocline. Surface data were not extracted above 3 dbar since air bubbles may have affected conductivity measurements.

Comparing the primary and secondary temperature sensors, a median difference of 0.003 ± 0.004°C was found, the primary sensor measuring warmer. Error bounds in all estimates are given as $\frac{\sigma}{\sqrt{n-1}}$. The surface offset of 0.004 ± 0.007°C was greater than the deep offset of 0.002 ± 0.005°C. These offsets were smaller than the errors and were not significant. Table A.4 summarizes the temperature cross-calibrations.

Table A.4: Primary – secondary temperature offsets

location	median	# samples (n)	std. dev. (σ)	mean ($\overline{x}$)	error ($\frac{\sigma}{\sqrt{n-1}}$)
Surface	0.004	19	0.032	0.005	0.007
Deep	0.002	159	0.060	0.002	0.005
Both	0.003	178	0.052	0.001	0.004

Post-cruise calibrations showed that both temperature sensors had drifted down by approximately 0.024°C. Since the TIWE cruises fall halfway between the calibrations, the measured temperature has been offset by +0.012°C to account for this shift. The SeaSoar data were comparable to the ADCP thermistor temperature data, although no cross-calibration is possible since the ADCP samples temperature at a shallower depth than the SeaSoar. As with the conventional hydrography data [Trefois *et al.*, 1993], laboratory calibrations appeared more stable than *in situ* comparisons with other instruments. No further calibrations were applied.

Comparisons between the primary and secondary conductivity sensors showed the

primary sensors measuring a median of 0.0013 ± 0.0007 Sm^{-1} lower than the secondary, as seen in Table A.5. This corresponds to a salinity error of 0.01 at a salinity of 34.25 and temperature of 25°C. The offset from the surface data only was 0.0017 ± 0.0052 Sm^{-1} and the offset from the deep data only was 0.0010 ± 0.0001 Sm^{-1}, suggesting little conductivity dependency.

Table A.5: Primary – secondary conductivity sensor offsets

location	median	# samples (n)	std. dev. (σ)	mean ($\overline{x}$)	error ($\frac{\sigma}{\sqrt{n-1}}$)
Surface	-0.0017	26	0.0266	-0.0086	0.0052
Deep	-0.0010	159	0.0032	-0.0012	0.0001
Both	-0.0013	185	0.0099	-0.0020	0.0007

A factory calibration was performed on the secondary conductivity sensor between MW9010 and MW9012. Since the quoted accuracy of this calibration was better than 0.0002 Sm^{-1}, the secondary sensor was considered the reference for TIWE-2. An offset of +0.0013 Sm^{-1} was applied to the primary conductivity data based on the above comparison.

Surface salinity bottles were collected from the ship when the SeaSoar was near the surface. The salinity data from these bottles measured 0.001 ± 0.015 lower than the primary sensors after the +0.0013 Sm^{-1} offset was applied. The surface SeaSoar measurement was taken at the time of the bottle collection only if shallower than 10 dbar. Using a shallower cutoff depth resulted in insufficient data points for comparison, while using a deeper one resulted in an increased offset due to stratification. Since the median offset was significantly below the error, no additional calibration was applied.

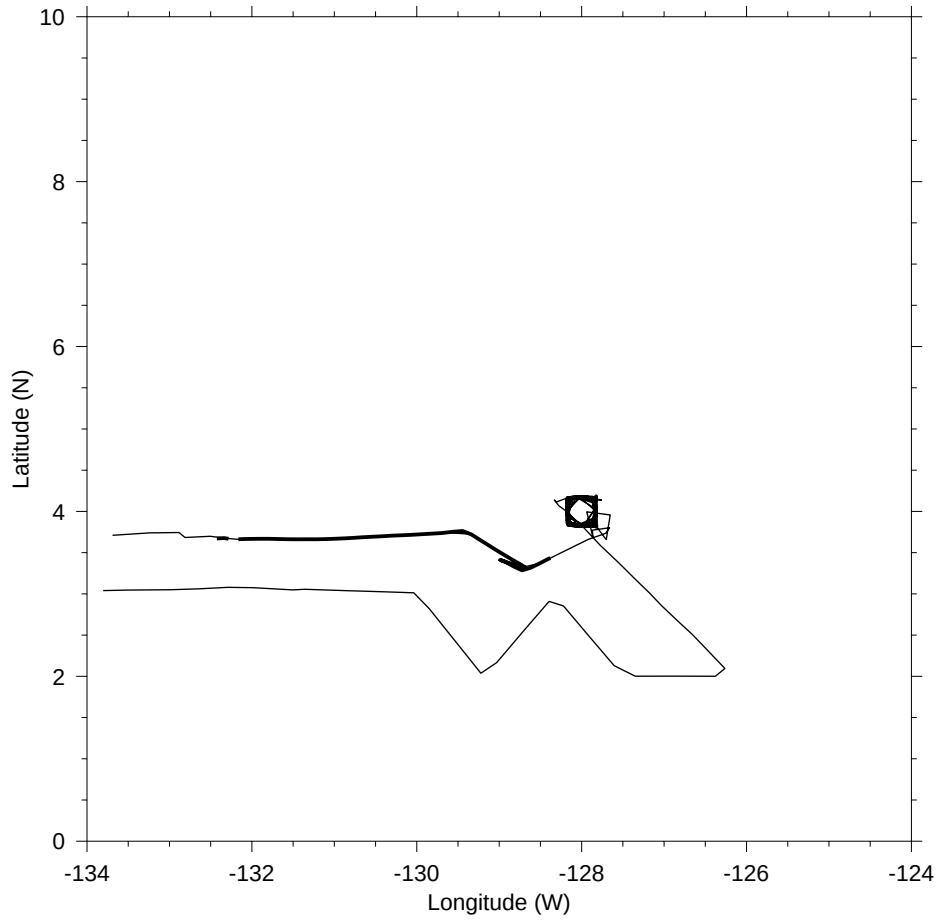

a

Figure A.1: Ship track during TIWE-1 (a) and TIWE-2 (b). Bold areas indicate SeaSoar deployments.

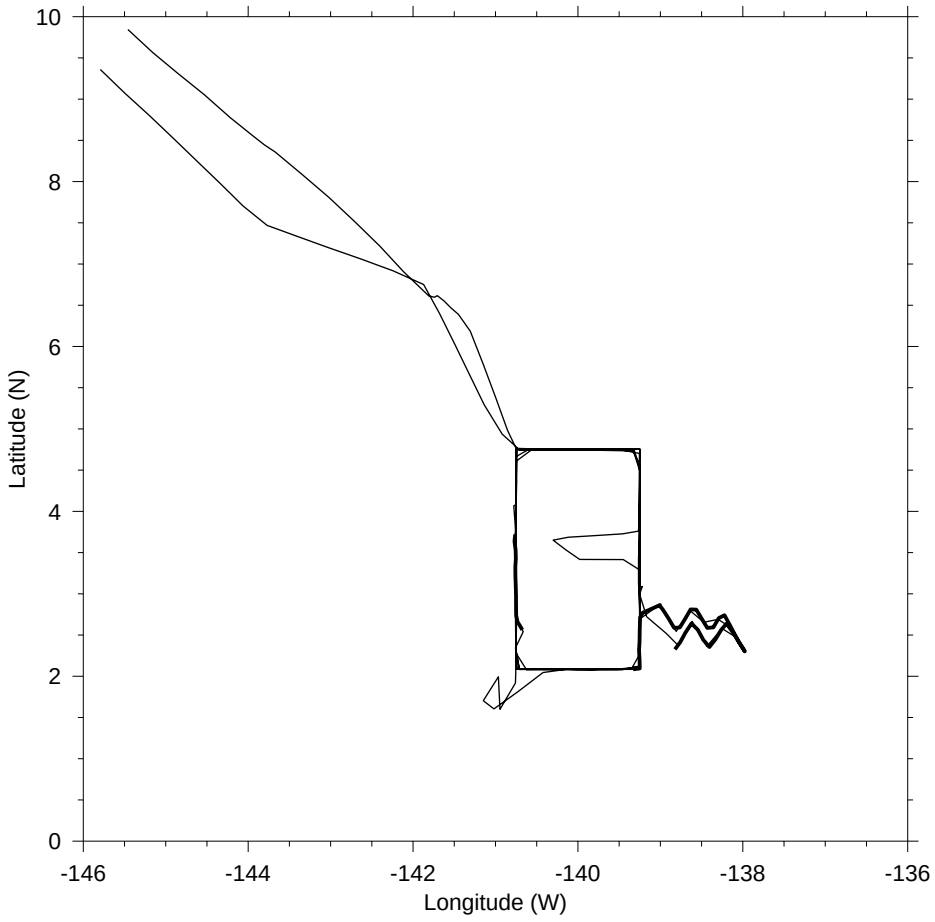

b

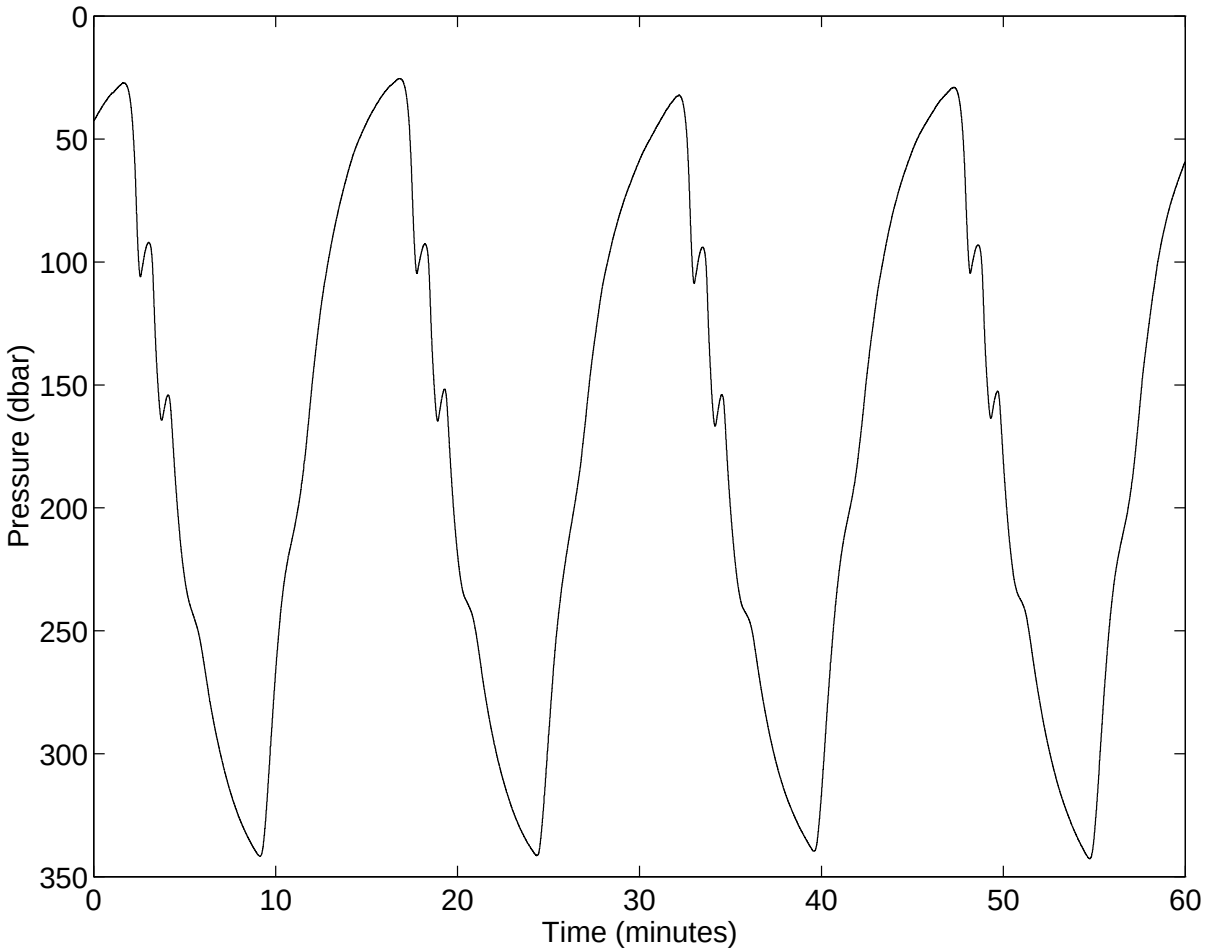

Figure A.2: Time-series of depth of SeaSoar for first hour of deployment on day 232. Note "hiccoughs" in downcast, as described in text.

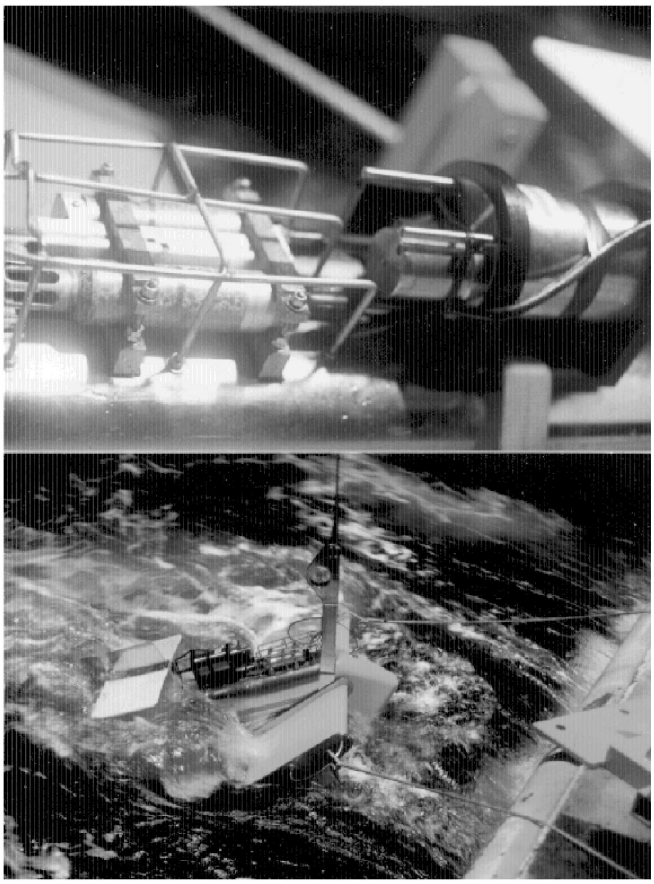

Figure A.3: Mounting configuration of the sensors during TIWE-1. The primary temperature and salinity sensors (indicated by T and S on the figure) were mounted just in front of the fluorescence sensor (indicated by F). Secondary temperature and salinity sensors were mounted inside the body of the SeaSoar.

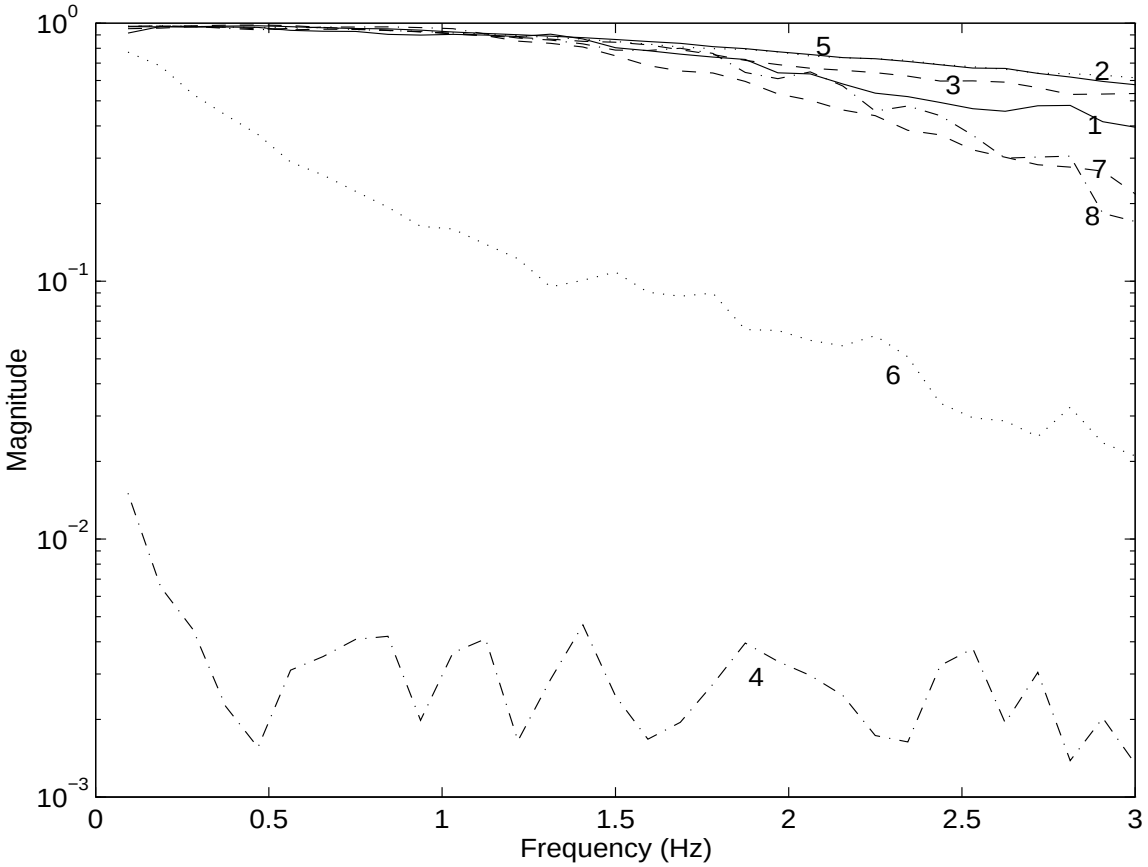

Figure A.4: Transfer function magnitude between primary conductivity C and "Modeled Conductivity" M (see text for details) for day 232.

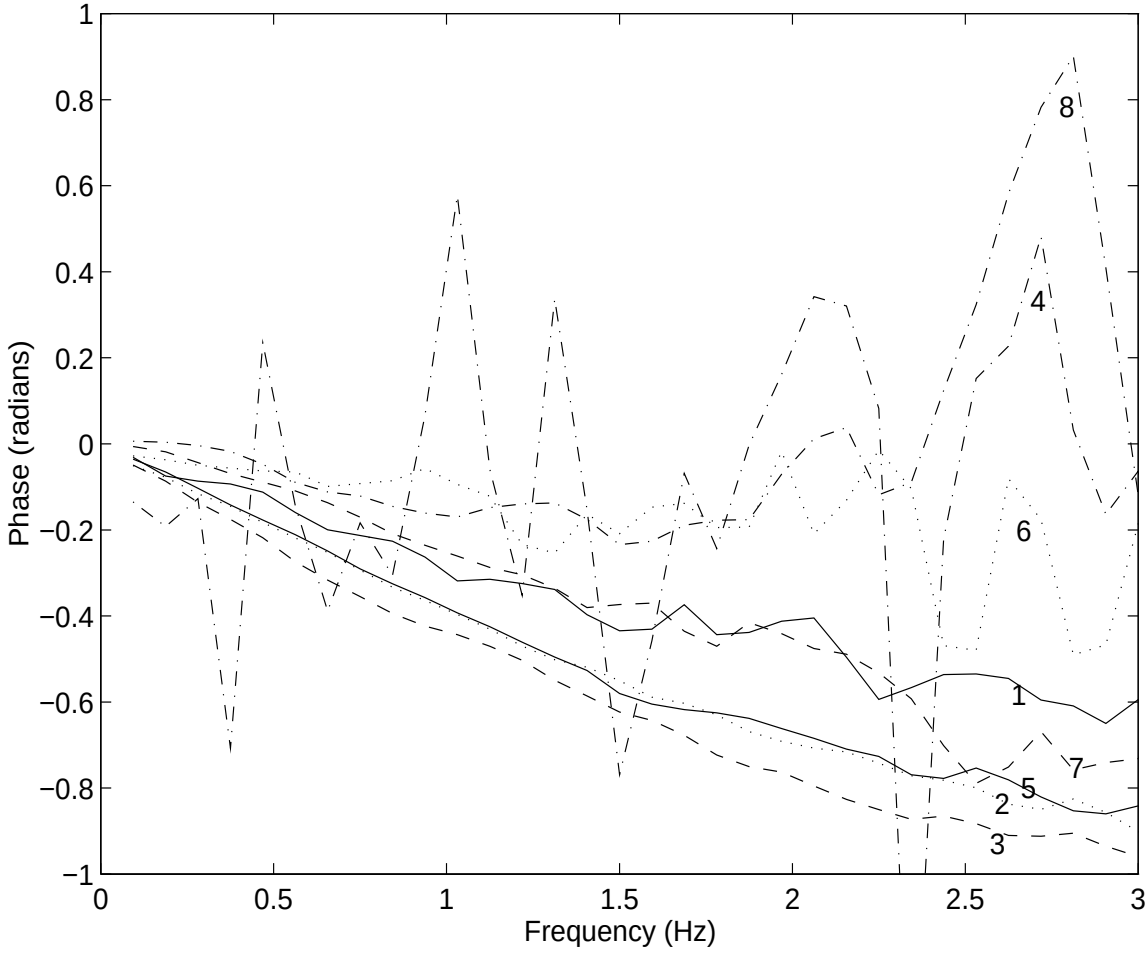

Figure A.5: Transfer function phase between primary conductivity C and "Modeled Conductivity" M (see text for details) for day 232.

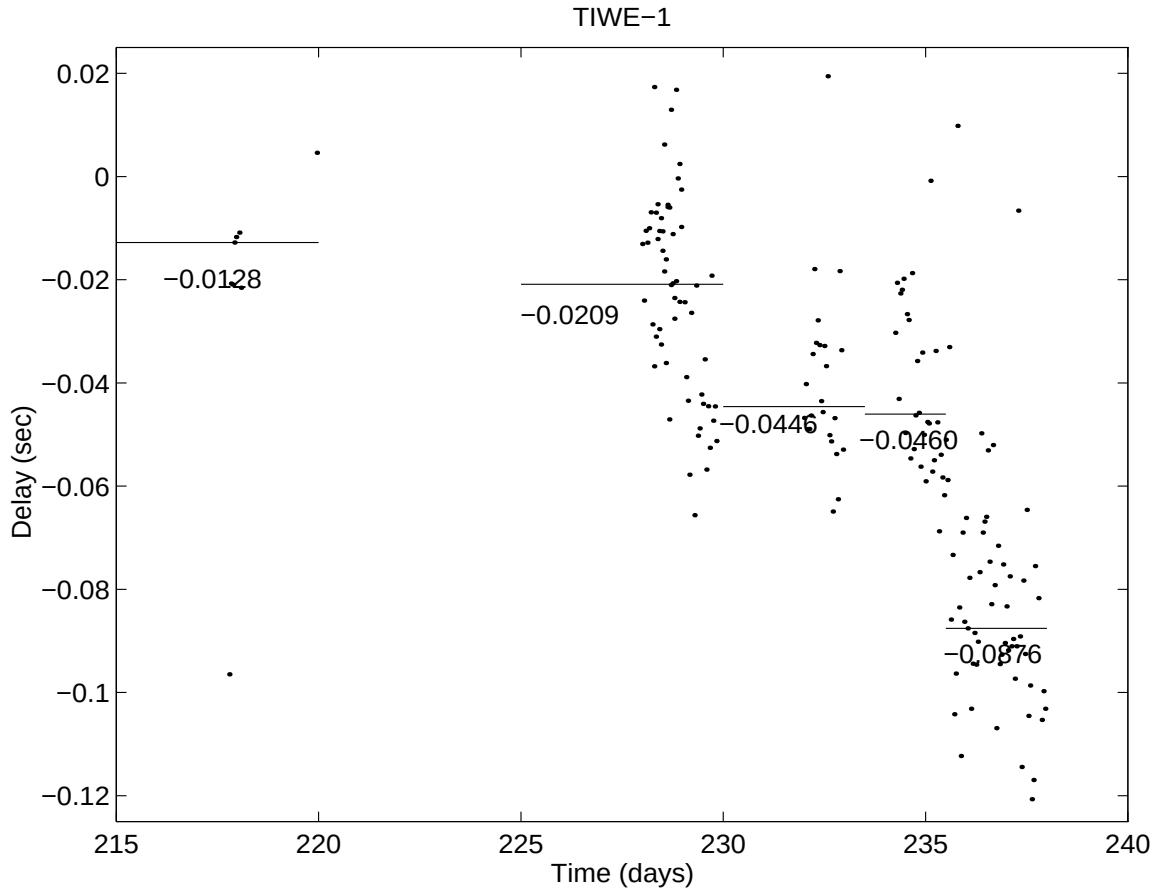

a

Figure A.6: Calculated delays between conductivity C and "modeled conductivity" M (see text for details) for MW9010(a), and MW9012(b). Negative values correspond to T lagging C. Labeled lines indicate median delays for individual SeaSoar deployments.

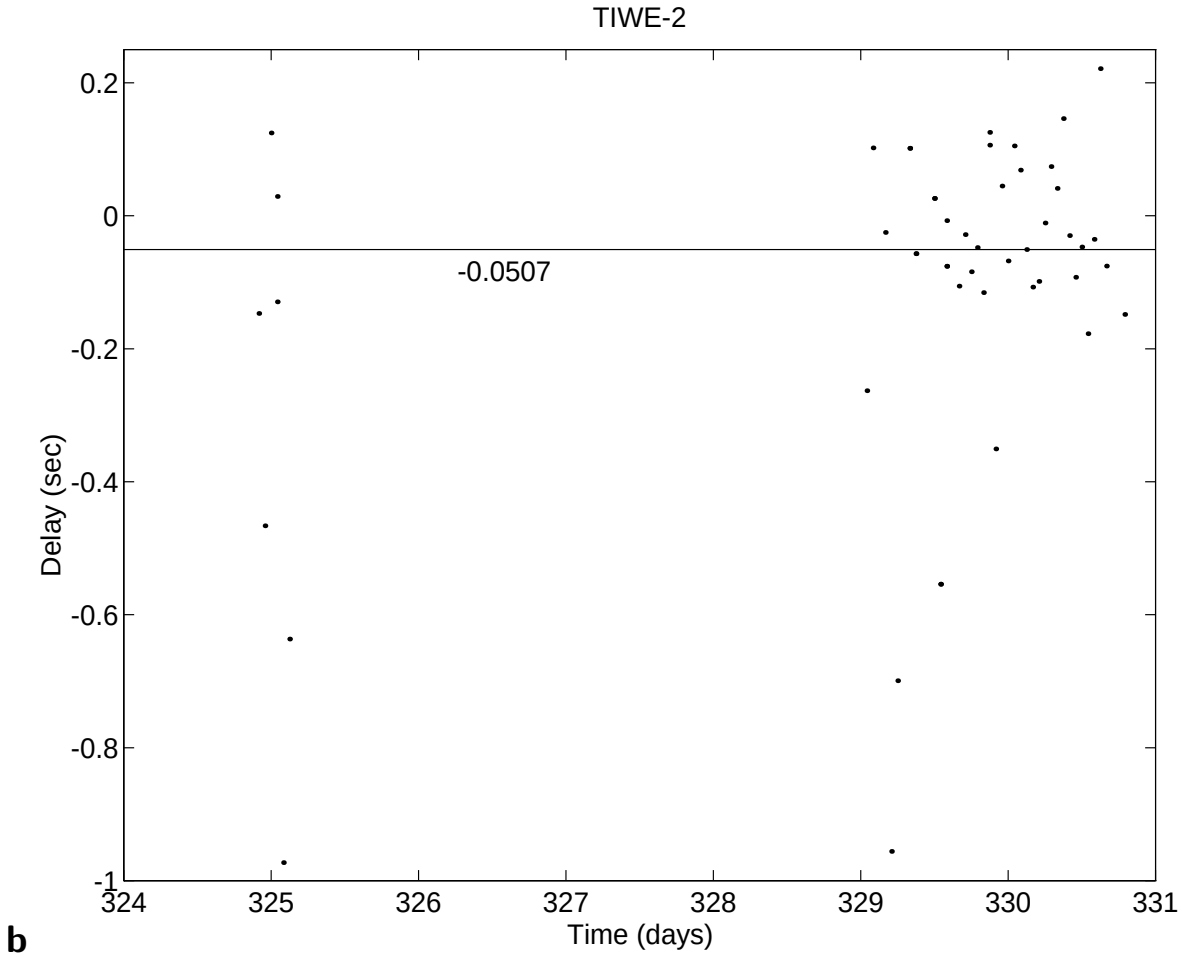
TIWE-2
0.2
0
-0.2
-0.4
-0.6
-0.8
-1
-0.0507
Delay (sec)
324
325
326
327
328
329
330
331
Time (days)

b

References

Chelsea Instruments, , (1987). *SeaSoar Handbook*. Unit 9, Avon Business Centre; Avonmore Rd. London W14 8TS.

Cox, M. D., (1980). Generation and propagation of 30-day waves in a numerical model of the Pacific. *J. Phys. Oceanogr.*, **10**, 1168–1186.

Cromwell, T., (1953). Circulation in a meridional plane in the central equatorial Pacific. *J. Marine Res.*, **12**, 196–213.

Düing, W., Hisard, P., Katz, E., Meincke, J., Miller, L., Moroshkin, K. V., Philander, G., Ribnikov, A. A., Voigt, K., and Weisberg, R., (1975). Meanders and long waves in the Equatorial Atlantic. *Nature*, **257**, 280–284.

Eriksen, C. C., Weller, R. A., Rudnick, D. L., Pollard, R. T., and Regier, L. A., (1991). Ocean frontal variability in the frontal air-sea interaction experiment. *J. Geophys. Res.*, **96**, 8569–8591.

Firing, J., Firing, E., Flament, P., and Knox, R., (1994). Acoustic doppler current profiler data from R/V Moana Wave cruises MW9010 and MW9012. Technical Report 93-05, School of Ocean and Earth Science and Technology, University of Hawaii at Manoa.

Flagg, C. N. and Smith, S. L., (1989). On the use of acoustic Doppler current profiler to measure zooplankton abundance. *Deep-Sea Res.*, **36**, 455–474.

Flament, P., Kennan, S. C., Knox, R., Niiler, P., and Bernstein, R., (1996). The three-dimensional structure of an upper ocean vortex in the tropical Pacific. *Nature*, **382**, 610–613.

Gill, A. E., (1982). *Atmosphere-Ocean Dynamics*, volume 30 of *International Geophysics Series*, chapter 7, Effects of Rotation, pages 189–245. Academic Press.

Hansen, D. V. and Paul, C. A., (1984). Genesis and effects of long waves in the equatorial Pacific. *J. Geophys. Res.*, **89**, 10431–10440.

Johnson, E. S. and Luther, D. S., (1994). Mean zonal momentum balance in the upper and central equatorial Pacific Ocean. *J. Geophys. Res.*, **99**, 7689–7705.

Johnson, E. S., (1996). A convergent instability wave front in the central tropical Pacific. *Deep-Sea Res.*, **43**, 753–778.

Kundu, P. K., (1990). *Fluid Mechanics*. Academic Press, Inc.

Legeckis, R., (1977). Long waves in the eastern equatorial Pacific Ocean: A view from a geostationary satellite. *Science*, **197**, 1179–1181.

Legeckis, R., (1986). Long waves in the equatorial Pacific and Atlantic Oceans during 1983. *Ocean-Air Interactions*, **1**, 1–10.

Luther, D. S. and Johnson, E. S., (1990). Eddy energetics in the upper equatorial Pacific during Hawaii–to–Tahiti Shuttle Experiment. *J. Phys. Oceanogr.*, **7**, 913–944.

Montgomery, R. B. and Stroup, E. D., (1962). Equatorial waters and currents at 150°w in july – august 1952. Technical Report 1, The John Hopkins University.

Niiler, P. P., Davis, R. E., and White, H. J., (1987). Water-following characteristics of a mixed-layer drifter. *Deep-Sea Res.*, **34**, 1867–1882.

Niiler, P. P., Sybrandy, A. S., Bi, K., Poulain, P. M., and Bitterman, D., (1995). Mea-

surments of the water-following capability of holley-sock and TRISTAR drifters. *Deep-Sea Res.*, **42**, 1951–1964.

Philander, S. G. H., (1978). Instabilities of zonal equatorial currents, 2. *J. Geophys. Res.*, **83**, 3679–3682.

Philander, S. G., (1990). *El Niño, La Niña, and the Southern Oscillation*, volume 46 of *International Geophysics Serie*, chapter 2, Oceanic Variability in the Tropics. Academic Press.

Philander, S. G., (1990). *El Niño, La Niña, and the Southern Oscillation*, volume 46 of *International Geophysics Serie*. Academic Press.

Trefois, C., Flament, P., Knox, R., and Firing, J., (1993). Hydrographic data from R/V Moana Wave cruises MW9010 and MW9012. Technical Report 93-01, School of Ocean and Earth sci and Technology, University of Hawaii at Manoa.

Tsuchiya, M., (1968). Upper waters of the intertropical pacific ocean. Technical Report 4, The John Hopkins University.

Weisberg, R. H. and Weingartner, T. J., (1988). Instability waves in Equatorial Atlantic Ocean. *J. Phys. Oceanogr.*, **18**, 1641–1657.

Yoder, J. A., Ackleson, S. G., Barber, R. T., Flament, P., and Balch, W. M., (1994). A line in the sea. *Nature*, **371**, 689–692.